UNIVERSITY OF CALIFORNIA
RIVERSIDE

Processing - Microstructure - Property Relationships of Novel Binary Nanocrystalline Alloys

A Dissertation submitted in partial satisfaction
of the requirements for the degree of

Doctor of Philosophy

in

Materials Science and Engineering

by

Anqi Yu

December 2021

Dissertation Committee:
Dr. Suveen Mathaudhu, Chairperson
Dr. Juchen Guo
Dr. Jianlin Liu

The Dissertation of Anqi Yu is approved:

Committee Chairperson

University of California, Riverside

Acknowledgements

I would like to firstly thank my PI Suveen Mathaudhu for providing professional advice to my projects and long-term support and help whenever I need it. He is not only an advisor but more like a parent to us all. He cares not only about our work but also our happiness and future career paths, just like we are his family members. I would also like to thank my mentor Christian Roach, who has guided me into metallurgical research when I joined UCR as a visiting undergraduate student in 2019. I also appreciate all the help and support from my colleagues at UCR, including Sina Shahrezaei, Trevor Clark, Heather Salvador, Erik Sease, Evander Ramos, Johny Quan, Madelyn Madrigal Camacho, Steven Herzberg, Yiwei Sun, Joshua Edwards, Adam Freund, Kendrick Mensink, Evanildo Vicente and Shelbi Salvador. We set up a "Grad Meeting" every week to help each other with any issue from lab safety to car maintenance, where I have gained a lot of support both physically and emotionally.

Also, I'd like to thank Professor. Lia Stanciu's group at Purdue University for casting Fe-30wt%Mn and sending it to the Mathaudhu group. And I am also grateful to Professor Kiran Solanki at ASU for providing the MTS mechanical tester and Dr. Karl. T. Hartwig at Texas A&M University for providing ECAE processing. My Cu-Ta project was supported by NSF (Collaborative Grant No. 1663522, Program Manager: Dr. Alexis Lewis (CMMI).

With the help and advice of Suveen, I joined PNNL in May 2021 as a PhD intern and gained a lot of help and support as well. I would like to express my great appreciation to

my mentor, Dr. Bharat Gwalani, for his professional knowledge and patience to help me with scientific thinking, technique skills at PNNL. I would like to thank my manager Tracy Baker, who checks on me every week to see if I need any help or have any questions. I would also like to thank Dr. Arun Devaraj and Dr. Aashish Rohatgi for their support and advice to help me fit in PNNL. Moreover, I'd like to thank my colleagues at PNNL, including Mayur Pole, Xiaolong Ma, Miao Song, Jia Liu, Elizabeth Kautz, Shuang Li, Tianhao Wang, and Mark Wirth. This work was supported by the Laboratory Directed Research and Development program at Pacific Northwest National Laboratory (PNNL) as part of the Solid Phase Processing Science initiative. A portion of this research was performed using facilities at the University of North Texas and Environmental Molecular Sciences Laboratory, a national scientific user facility sponsored by the U.S. Department of Energy's (DOE's) Office of Biological and Environmental Research and located at PNNL. PNNL is a multiprogram national laboratory operated by Battelle for the DOE under Contract DEAC05-76RL01830. SP and SV acknowledge funding from NSF MRI #1726897 and DOE DE-NE0008739 for this work.

ABSTRACT OF THE DISSERTATION

Processing - Microstructure - Property Relationship of Novel Binary Nanocrystalline Alloys

by

Anqi Yu

Doctor of Philosophy, Graduate Program in Materials Science and Engineering
University of California, Riverside, December 2021
Dr. Suveen Mathaudhu, Chairperson

Nanocrystalline (NC) metals have sparked an increasing number of research interest due to their superior mechanical properties as compared to their coarse-grained (CG) counterparts. Such enhanced mechanical properties of NC alloys can vary significantly depending on their microstructures, which are affected by their processing routes and deformation mechanisms. As a result, it is more than significant to study the processing - microstructure - property relationship in novel binary NC alloys. In this dissertation, this relationship is addressed in both engineering perspective and science perspective.

The engineering perspective involves the mechanical and bio performance of Fe-Mn alloys as a function of processing routes and microstructural evolution. Although coarse-grained Fe-based alloys as a bioresorbable material have been well studied, there is a knowledge gap on how the microstructures affect corresponding mechanical/bio response. Therefore, in this study we used high pressure torsion to refine the grain size of Fe-30wt%Mn, and spark plasma sintering to create a nano-porous structure. The advanced mechanical strength after HPT and improved degradation rate by porous structure in NC Fe-Mn alloys show that the material can be optimized by tailoring parameters during processing and fabrication.

The science perspective focuses on microstructurally stable Cu-based immiscible NC alloys. In the field of thermal stability of NC materials, less effort has been devoted to the investigation of current-based sintering approaches for consolidation. Also, the independent contribution of shear strain and temperature on the microstructural evolution in this type of microstructurally stable, Cu-based immiscible NC alloys have not been well addressed. Therefore, in my work, we studied the microstructural evolution in Cu-Ta alloy powders during SPS consolidation with particular attention to the microstructural evolution and to the effects on strengthening, and we used a pin-on-disk tribometer to study the microstructural evolution of Cu-Nb alloys to shear strain and temperature separately. NC Cu-Ta alloys made by SPS exhibited a thermomechanical stability, which is explained by observed bimodality of Ta segregates. Also, the effect of shear strain and temperature are decoupled in the tribometer test, showing grain refinement caused by severe shear

deformation, as well as grain growth/recrystallization and strain relaxation caused by external heating.

Table of Contents

List of Figures

List of Tables

Introduction

Nanocrystalline (NC) metals, which are defined as metals containing grain sizes below 100 nm in at least one dimension, have attracted an increasing number of studies, both experimental and computational [1]. These NC metals and their alloys have exhibited superior mechanical properties as compared to their coarse-grained (CG) counterparts, such as increased strength, higher wear resistance and toughness [2, 3]. These attractive properties of NC metals lead to extensive research interest in microstructural evolution during deformation, as well as the corresponding mechanical properties. For some novel binary NC alloys, the microstructures and mechanical properties can be controlled to fit specific engineering applications. For example, W-Ti NC alloys can be designed to obtain a stable nanostructure even at high temperatures, overcoming the drawback of microstructure instability due to small grain size for NC alloys [4]. Ni-Ag NC alloys can be customized to achieve a high cycling wear resistance which enables it to be used under high cyclic load conditions [5]. Such enhanced mechanical properties of NC alloys can vary significantly depending on their microstructures, which are affected by their processing routes and deformation mechanisms. For example, the tensile strength of the W NC alloy processed by HPT can be twice as high as the same alloy processed by Equal Channel Angular Pressing (ECAP) and rolling [6]. In addition, the ductility of NC Cu can be as low as less than 3% when fabricated by surface mechanical attrition treatment [7] or as high as 30% when processed by a special method combining room temperature milling and cryomilling [8]. As a result, it is more than significant to study the processing - microstructure - property relationship in novel binary NC alloys.

This dissertation addresses this relationship in both engineering perspective and science perspective by studying bioresorbable NC Fe-Mn alloy system and immiscible NC Cu-base alloy system, respectively.

Fe-Mn alloys have been recognized with a new application for making bioresorbable implants due to the combination of their promising mechanical strength and bioresorbability [9, 10]. For mechanical strength, microstructure evolution of high Mn steel processed by HPT has shown that the deformation twins and deformation bands increased the yield strength by acting as obstacles to dislocation movement [11, 12]. In addition, martensitic transformation (transition from austenitic γ phase to martensitic ε phase) in Fe-Mn alloys increases the strength of the alloy by accumulation of dislocations [13, 14]. For bioresorbability, Fe has been tested as an effective bioresorbable metal considering the safety, cell attachment and proliferation, and thrombogenicity [15], and alloying iron with manganese both decreases the thrombosis potential and increases the degradation rate [16]. However, although coarse-grained Fe-based alloys as a bioresorbable material have been well studied [15-17], there is a knowledge gap on how the microstructural evolution mechanisms affect corresponding mechanical/bio response, as well as how the porous structures of the material affect the degradation rate in Fe-Mn in nanoscale compared with their coarse-grained counterparts. Therefore, in this study I used high pressure torsion (HPT), a sufficient deformation technique [18], to refine the grain size of Fe-30wt%Mn to tailor the mechanical strength and degradation rate, as well as reducing the risk of blocked blood vessels. By processing the material with various turns of HPT, In addition, I used

spark plasma sintering (SPS), an advanced consolidation process [19], to fabricate a nano-porous Fe-Mn alloy and tailor the porosity by controlling the processing parameters.

Despite of superior properties of NC alloys compared to their coarse-grained counterparts [20], most NC materials suffer deleterious grain growth caused by diffusional creep, grain boundary sliding and rotation, at elevated temperatures or under mechanical loads [21], presenting challenges to the application of NC alloys in applied conditions, such as the aerospace, naval, civilian infrastructure and energy sectors [22]. Fortunately, thermally stabilized nanostructured materials have shown promise for overcoming the detrimental grain growth that often occurs at high homologous temperatures in conventional nanocrystalline alloys. And in the field of thermal stability of NC materials, researchers have primarily fabricated materials with cryomilling plus severe plastic deformation densification [23, 24], or thin-film synthesis approaches [25]. But less effort has been devoted to the investigation of current-based sintering approaches for consolidation. More specifically, there is a lack of knowledge of the retention of thermal stability and resultant microstructures that occur during SPS. Therefore, in my work, we will parametrically study the microstructural evolution in thermally stabilized Cu-Ta alloy powders during SPS consolidation with particular attention to the microstructural evolution and to the effects on strengthening.

After this type of thermomechanical stable immiscible alloy system is fabricated, it is always important to study their response to temperatures and severe deformations. Solid phase processing (SPP) of immiscible alloys involving high shear strain and processing-generated heat results in peculiar microstructures and outstanding properties of materials

[26-28]. Researchers have shown that severe shear deformation during SPP of metals and alloys results in microstructural refinement assisted by grain rotation [29], dislocation assisted plastic deformation [30], self-organization of second phase [31], and often shear induced atomic mixing [32, 33]. In contrast to microstructural refinement, grain growth has also been observed in some SPP cases because deforming the material releases energy that causes the temperature to rise , which could directly impact the transformation pathways during deformation [34, 35]. However, because the local heating is produced by the processing itself and uncontrollable, there is a lack of a full understanding of independent contributions of strain and temperatures in immiscible alloy systems. As a result, in this study a pin-on-disk tribometer is used at various temperatures to mimic SPP since the processing-induced local heating can be assumed to be negligible in this tribometer technique compared with SPP.

In summary, this dissertation is expected to offer a better understanding of mechanical strength and degradation rate as a function of grain size and microstructural evolution of Fe-Mn alloys, thermomechanical stability and strengthening mechanism as a function of hierarchical microstructure in Cu-Ta alloys, as well as decoupled shear strain effects and temperature effects in Cu-Nb alloys.

Chapter 1: Microhardness and Microstructural Evolution in Nanocrystalline Fe-30wt%Mn during High Pressure Torsion

1.1 Abstract

The microhardness and microstructural evolutions of Fe-30wt%Mn samples deformed by high pressure torsion (HPT) for one, two and four turns were investigated. HPT was used to refine the microstructure by fragmenting large columnar grains into dislocation cells which then form nano-scale grains. Possible strengthening model is discussed in this study, and the grain refinement, high dislocation density and deformation twinning caused by the severe plastic deformation are considered responsible for significant strengthening of Fe-30wt%Mn after HPT.

Keywords: grain refinement, martensitic transformation, deformation twinning

1.2 Introduction

Fe-Mn alloys have gained interest due to their excellent mechanical properties, including a combination of strength and ductility [9] and potential biomedical applications [10] The attractive mechanical properties of these alloys at the engineering level can be explained by their complex microstructures. For instance, microstructure evolution of high Mn steel processed by HPT has shown that the deformation twins and deformation bands increased the yield strength by acting as obstacles to dislocation movement [11, 12]. In addition, martensitic transformation (transition from austenitic γ phase to martensitic ε phase) was observed during plastic deformation in Fe-Mn alloys [13]. It was found that martensitic plates which formed in the austenitic steel by plastic deformation increased the strength of the alloy by accumulation of dislocations [14]. The ductility of Fe-Mn alloy is

accommodated by the transformation induced plasticity (TRIP) and twinning induced plasticity (TWIP), causing extensive local strain hardening [36]. Therefore, it is more than important to have a systematic understanding of the microstructural evolution during the deformation processes that results in optimum mechanical properties.

The purpose of present work is to study the effect of HPT on microhardness and microstructural evolution of nanocrystalline Fe-30wt%Mn. Casting, homogenization, and HPT are used to produce a nano-grained sample. Homogenization are required to remove the heterogeneity of the as-cast samples caused by high volume fraction of dendrites. Visible-light Microscopy, Scanning Electron Microscopy (SEM) and Transmission Electron Microscopy (TEM) are applied to study the evolution of microstructure during HPT. X-ray diffraction (XRD) is applied to study the phase evolution and estimate grain size of Fe-30wt%Mn samples processed by HPT. In the meantime, Vickers indentation is used to test the microhardness of the samples.

The visible-light microscopy and the SEM images show that the dendritic structures are almost gone after the homogenization process, indicating that the as-received Fe-30wt%Mn samples are successfully homogenized. The X-ray diffraction patterns confirm martensitic transformation in Fe-30wt%Mn during HPT, which becomes more pronounced after two turns of HPT. Moreover, Scherrer's equation [37] is used to estimate grain size of Fe-30wt%Mn after varying turns of HPT, based on a Full Width at Hall Maximum (FWHM) approximation of the austenite (111) peak. The grain sizes estimated by Scherrer's equation are 22 nm, 11 nm and 13 nm for Fe-30wt%Mn samples after one, two and four turns of HPT, respectively. Although some errors are unavoidable during these

estimations, such as machine or measurement variations, it provides evidence that grain refinement is achieved by HPT.

Although high density of dislocations makes it difficult to observe clear grain boundaries, nano-sized microstructures, such as nano-sized dislocation cells, nano-twinning and martensitic plates can still indicate the presence of grain refinement. In addition, twinning diffractions and nano-twinning are observed in TEM images, which is expected due to the low stacking fault energy of Fe-30wt%Mn steels [38]. The Vickers hardness of Fe-30wt%Mn was found to increase significantly, from 0.98 GPa to 6.28 GPa after one turn of HPT. However, an unexpected decrease of Vickers hardness is observed after two turns of HPT. Although the hardness increased to 6.35GPa after four turns of HPT, the hardness of Fe-30wt%Mn after one, two and four turns are within error margins of each other. One possible reason for this observation might be explained by saturation of dislocations or recrystallization during HPT.

1.3 Materials and Methods

1.3.1 Materials

The as-cast Fe-30wt%Mn samples (10mm in diameter and 1.2mm in thickness) are fabricated in similar fashion to Dr. Stanciu's paper [10].

1.3.2 Homogenization of as-cast Fe-30wt%Mn

All samples were sealed in a quartz tube under vacuum in the presence of titanium getter to prevent oxidation. The samples were put in a ST-1700C-888 High Temperature Box Furnace (Sentro Tech Corp) and heated to 1100 ℃ at a heating rate of 30 ℃/min under an

Argon atmosphere. Afterwards, samples were held at 1100 ℃ for 48 h before cooling to room temperature at the same rate.

1.3.3 Deformation processing

In this study, the HPT device was custom-made. The main components of the HPT device were composed of the upper anvil, sample and the lower anvil [39]. During the experiment, samples were placed between the upper anvil and lower anvil. These two anvils applied a pressure of 6 GPa on the sample while the lower anvil rotated with the speed of 40s/turn at room temperature.

1.3.4 Characterization

All samples were mechanically ground to 1200 grit, then further polished with alumina and colloidal silica, rinsed with isopropanol and air dried before being chemically etched via Nital solution (2% HNO_3 in methanol). Visible-light microscopy was performed to examine the microstructures after each processing step, and SEM (Nova NanoSEM 450) with concentric backscattered detector (CBS) was used to examine the microstructure of the Fe-30wt%Mn samples. Transmission Electron Microscopy (FEI Tecnai T12 TEM) was utilized to observe the microstructure of Fe-30wt%Mn after HPT. The TEM sample was prepared using Focused Ion Beam (FIB, Scanning DualBeam Microscope Quanta 3D 200i). X-ray diffraction (PANalytical Empyrean Series 2) was used to study the phases and grain size of samples.

1.3.5 Hardness Test

Vickers Hardness for materials were measured using Micro Vickers Hardness Tester (Phase II, model no.900-391) equipped with optical microscope, under 1 kgf load with

dwelling time of 15s. 8 measurements were recorded for each sample, with 1 mm spacing between subsequent indents.

1.4 Results

Figure 1.1 (a) and (c) show a large volume of dendrites in the as-cast Fe-30wt%Mn, causing heterogeneity that would make HPT process difficult. Therefore, all samples were homogenized at 1100 ℃ for 48h, with the resulting microstructure shown in Figure 1.1 (b) and (d). After homogenization, grains are columnar with a width of approximately 200 μm, as shown in Figure 1.1 (d). The homogenized Fe-30wt%Mn were processed by HPT under 6 GPa pressure for one, two and four. The effective applied shear strain γ is estimated according to [40]:

$$\gamma = \frac{2\pi N r}{\sqrt{3}h} \tag{1.1}$$

where N is the number of turns, r is the sample radius, and h is the sample thickness. The shear strain calculated with the equation after HPT reaches values of 18, 36 and 72 at the sample edge for one, two and four turns, respectively. These values are used here only as qualitative analysis for the maximum possible shear strain value.

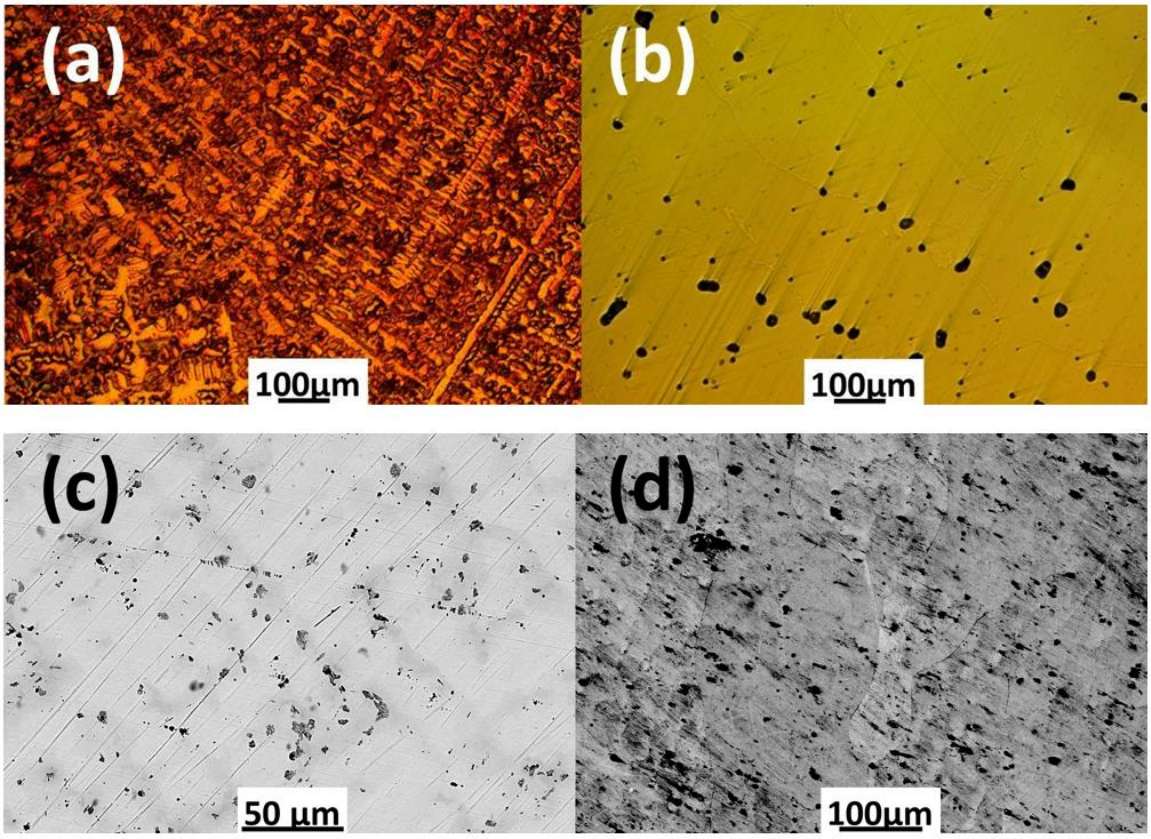

Figure 1.1 The Visible-light Microscopy of the as-cast Fe-30wt%Mn (a) and the homogenized Fe-30wt%Mn (b); the backscattered SEM image of the as-cast Fe-30wt%Mn (c) and the homogenized Fe-30wt%Mn (d).

Figure 1.2 shows the X-ray patterns of Fe-30wt%Mn before and after HPT with different numbers of turns. The grain size of Fe-30wt%Mn was estimated through Scherrer Analysis [40] according to the Full Width at Half Maximum (FWHM) of an enlarged γ-austenite peak in Figure 1.2 (b) and the grain size results are given in Figure 1.2 (a). The analysis yielded an average grain size of 22 nm for Fe-30wt%Mn after one turn, 11 nm for that after two turns and 13 nm for that after four turns, respectively. It is worth mentioning that there can be errors from the machine and operation procedure, causing the data to be semi-quantitative reliable. Peaks shifting to the right in Figure 1.2 (b) is caused by residual strain.

It is noteworthy that the <220> orientation is not stable, and its intensity decreased significantly after one turn of HPT. The decreased peak intensity of γ (220) and increased peak intensity of γ (200) mean that texturing occurred after one turn of HPT, but it is not obvious after two turns and four turns of HPT. Grain subdivision accompanied by a strong texture evolution can lead to a very significant increase in the fraction of high angle boundaries in a deformed metal [41]. In addition, the increased martensite (ε) peak at around 47 ° and the decrease of austenite peaks indicate that there is a martensitic transformation induced by HPT. The martensitic transformation is also confirmed by TEM images as discussed below.

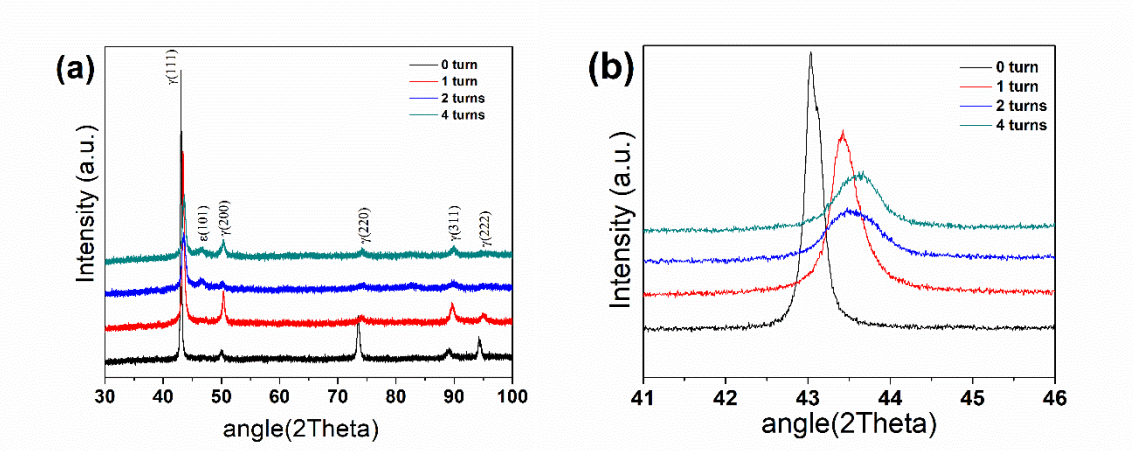

Figure 1.2 X-ray diffraction patterns of Fe-30wt%Mn before and after HPT with different numbers of turns (a), and the enlarged γ-Austenite peak at ~ 43 degree.

The microstructure of a severely deformed Fe-30wt%Mn sample processed by HPT for two turns was further investigated by TEM and corresponding micrographs as well as the selected area diffraction patterns (SADP), as shown in Figure 1.3. The dark-field TEM image at the bottom left corner of Figure 1.3 (a) taken at a matrix diffraction spot clearly reveals fine particles which are randomly distributed with an average size of about 100 nm.

It is difficult to observe clear grain boundaries in TEM images because of high density of dislocations, as shown in Figure 1.3 (c) and (d). However, subgrains and dislocation cells of about 200 nm in size in a deformation band are shown in the bright-field TEM image in Figure 1.3 (c). Therefore, it is reasonable to assume that large columnar grains are fractured by the large strain induced during HPT. The shear strain tears the long grain apart into smaller dislocation cells. When the dislocation cells are completely separated from each other by further deformation, they will become nano-scale grains. This assumption is supported by Hansen et al., who claimed that the evolution of dislocation structure in polycrystals with increasing strain is described within a framework of grain subdivision boundaries and high angle boundaries [42]. It is noted that dense dislocation walls and the deformation band in Fe-30wt%Mn after two turns of HPT are inclined at an angle of about 50 °. While the measured boundary misorientation in Al, Ni, and Ta are distributed from nearly 0 to 62.8 ° [43]. The bright-field images and the dark-field image indicate an obvious grain refinement achieved by HPT in Fe-30wt%Mn, compared with the grain size of the homogenized sample shown in Figure 1.1 (d).

In addition, nano-twinning diffractions are found in the SADP graph in Figure 1.3 (b), which are indicated by the white arrows. The bright-field image, as shown in Figure 1.3 (c), indicates very thin nano twinning microstructure and a straight nano twinning boundary, which is similar to the observed nano-twinning in a 20% compressed Fe-33wt%Mn-2.97wt%Al-3wt%Si [44].. The twinning activity may be influenced either by the crystal orientation or by the amount of applied strain. On the one hand, an increase of strain should initiate twinning in grains with orientations initially favoring slip, which is

mostly (111) direction [41]. Based on the X-ray patterns, the peak intensity of austenite γ (111) decreases as the applied strain increases, making it difficult to predict the formation of nano-twinning in Fe-30wt%Mn. On the other hand, texture formation may reduce the twinning-preferred orientation space [41]. According to the X-ray diffraction pattern, texturing in Fe30wt%Mn only occurred after one turn of HPT. However, the peak intensity of austenite γ (111) is the highest among different turns of HPT tested. Therefore, there is a balance of twinning formation and twinning annihilation.

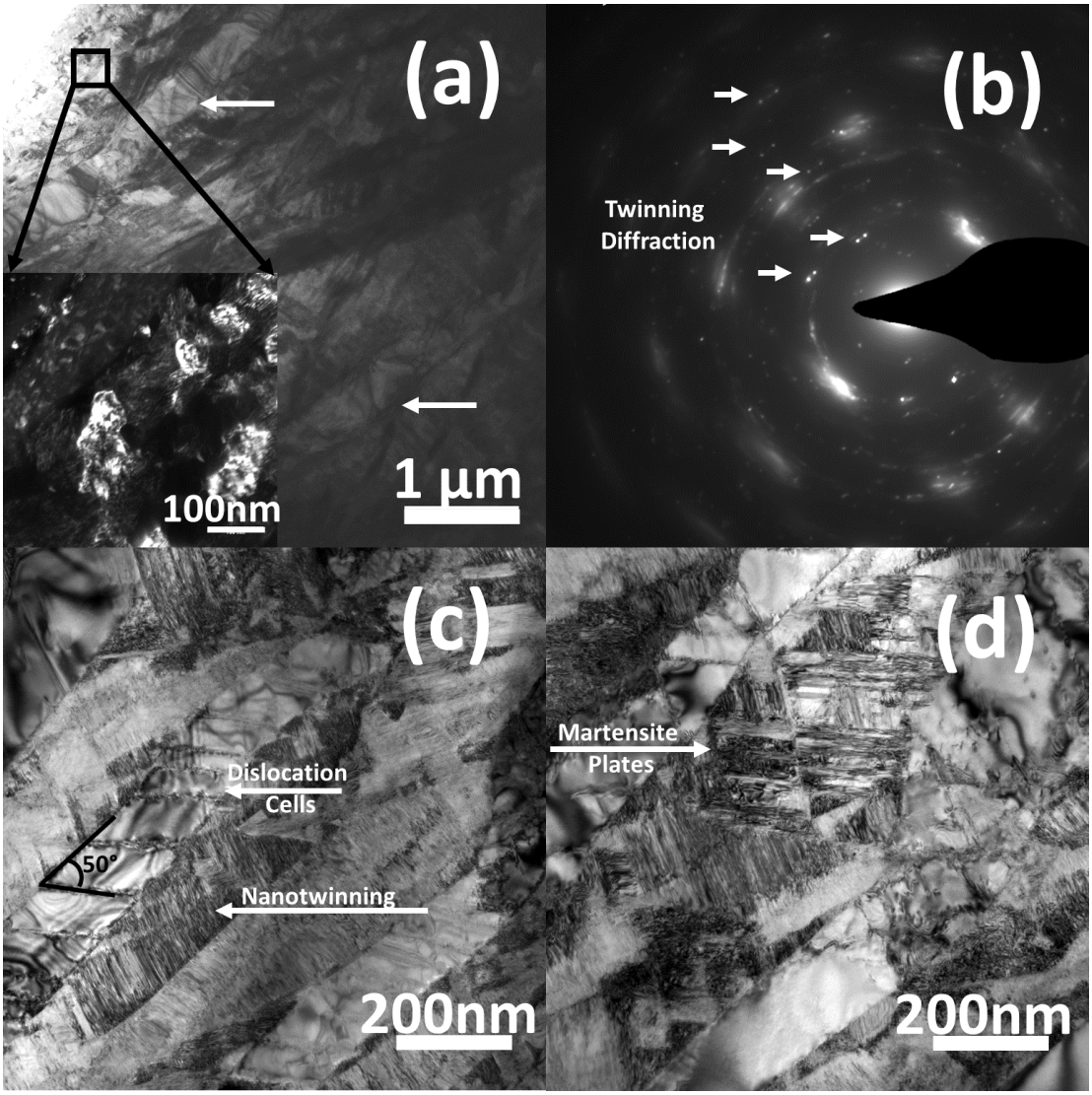

Figure 1.3 Bright-field TEM micrographs of Fe-30wt%Mn after two turns of HPT incorporated with an enlarged dark-field TEM graph on the matrix at the bottom left corner (a), the corresponding diffraction pattern of the matrix (b), bright-field TEM image showing dislocation cells and thin nano-twinning (c), and martensite plates (d).

Figure 1.3 (d) shows martensite plates consisting of high-density dislocations, which support the martensitic transformation result observed in the X-ray patterns. It was found that martensite plates formed in austenitic steel by plastic deformation increased the strength of the alloy by accumulation of dislocations [14]. The martensite plates in Figure

1.3 (d) are showing much finer microstructures than their periphery area. The high density of dislocations shown in martensite plates can act as obstacles for dislocations to glide or rotate. The strain-induced martensite formation is known to increase the tensile strength through a progressive generation of a harder phase [45]. Therefore, it is expected that the appearance of martensite plates would increase the microhardness of Fe-30wt%Mn in this study.

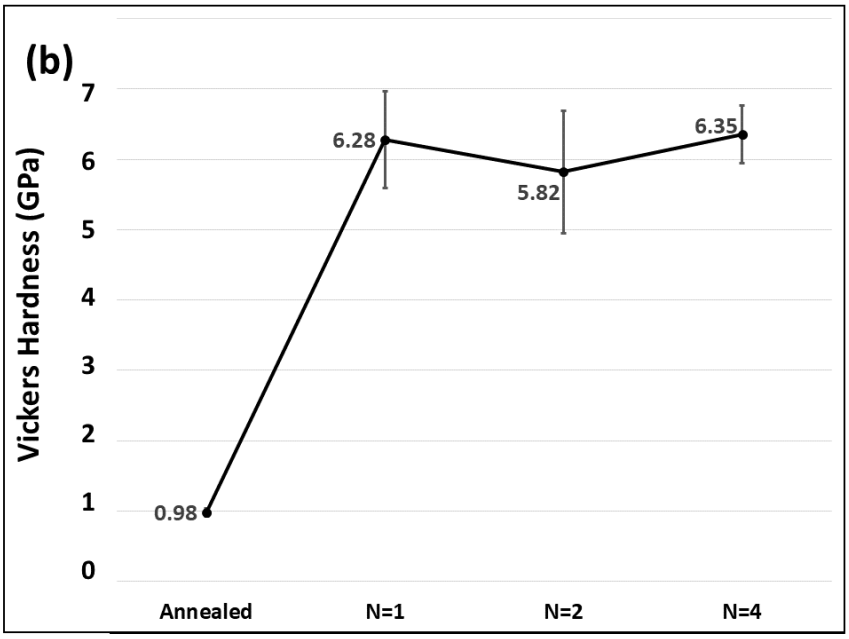

Figure 1.4 Vickers hardness results of Fe-30wt%Mn before and after HPT. "N" represents the turn number of HPT.

Plastic deformation of metals is reflected in the microstructure and texture, which determines their mechanical behavior. The previously described changes in the microstructure are also reflected in changes of the measured microhardness. In Figure 1.4, the hardness increases significantly from a value of 0.98 GPa in the homogenized sample up to 6.28 GPa for the sample after one turn of HPT. The relatively low microhardness

(0.98 GPa) is the result of large grains; and the low standard deviation is due to the lack of hardness variation between the dendrites and inter-dendritic regions in the homogenized sample. It is not a surprise that the microhardness of Fe-39wt%Mn can be enhanced significantly based on the nano-twinning and martensitic transformation observed in the X-ray patterns and micrographs. The microhardness of Fe-30wt%Mn after various turns is within error margin. Although microhardness of Fe-30wt%Mn increases significantly after HPT, the hardness behavior in these experiments is unusual because in many materials, including Fe-based alloys, the hardness increases with increasing numbers of turns and then saturates after a certain amount of turns [46, 47]. In the present experiments, the microhardness increased from the homogenized status but it was slightly higher after one turn than after two turns. Two reasons are usually used to explain this anomalous phenomenon. The first reason can be the recrystallization caused by the heat generated during the HPT process. A study by Edalati et.al. observed the effects of HPT on pure Mg and found a decrease of ultimate tensile strength as the number of turns approaches 10, along with an observed recrystallization in these samples [48]. The second reason may be that this hardness saturation was not reached after one turn of HPT. Based on the standard deviation shown in Figure 1.4, the microhardness of Fe-30wt%Mn after one, two and four turns are quite close to each other. The slight difference can be caused by errors in measuring procedure or by the heterogeneity of Fe-30wt%Mn after HPT.

1.5 Discussion

1.5.1 Microstructural evolution

HPT leads to the fragmentation of initial columnar grains mainly due to the formation of a high dislocation density, martensitic lathes, twins and localized deformation bands, as shown in Figure 1.3. In addition, Fe-30wt%Mn processed after 2 turns of HPT shows a lamellar structure with alternative phases – one is the austenite phase composed of dislocation walls and nanotwins, another phase is the martensite lathes. Based on the microstructure evolution and X-ray patterns above, the actual reason for the abnormal microhardness behavior can be much more complex.

After one turn of HPT, texturing occurs in Fe-30wt%Mn by compression and torsional strain from HPT, which makes the grains glide or rotate easier along the lateral orientation. Therefore, when Vickers indents are applied on the surface of the sample, it faces more resistance, and the sample appears harder than the homogenized one. Besides, it is reasonable to conclude that nano-twinning has been formed since one turn of HPT because there is a relatively high austenite γ (111) XRD peak that favors twinning. The fine nano twinning boundaries can act as obstacles to prevent dislocation movement, thereby significantly increasing that microhardness.

It is known that transformation induced plasticity and twinning induced plasticity are competitive in high-Mn steels depending on the stacking fault energy [36, 49, 50]. Although both nano-twinning and martensitic transformation are confirmed by X-ray patterns and TEM images after two turns of HPT, the martensite ε peak intensity is relatively low, indicating that the influence of martensitic transformation on microhardness

is mild, and nano-twinning plays a much more important role. The small fractions of martensite phases could be the result of severe plastic deformation by HPT and some local inhomogeneity in the chemical composition in the single crystals, which is difficult to remove by the homogenization process. Since the microhardness of Fe-30wt%Mn didn't increase after two turns of HPT, it is safe to say that nano-twinning formation is prevented or annihilated. The peak intensity of slip-favored austenite γ (111) has decreased significantly after two turns of HPT, leaving less grains which favors twinning formation. In addition, the dense dislocation shown in Figure 1.3 (c) and (d) indicates a possible dislocation saturation, which prevents the microhardness to be increased. It is also possible that a small amount of recrystallization occurred after two turns of HPT caused by the friction between the sample and the device during HPT. There is no significant difference in microhardness of Fe-30wt%Mn after four turns of HPT, which further confirms that dislocation saturation has been achieved.

Although similar hardness results of Fe-30wt%Mn after different number of turns for HPT are shown in Fig. 4, the standard deviation is the smallest when the sample is under four turns of HPT, indicating that HPT is not only increasing the hardness of the sample but also increasing the homogeneity of the hardness. The results are reasonably consistent with Dr. Kashyap's results [51] that an austenitic steel was hardened by HPT with a higher homogeneity when it is under more turns.

1.5.2 Strengthening mechanisms

Assume that the enhanced microhardness H is contributed by the solid solution strengthening, grain boundary strengthening, dislocation density strengthening and twin

boundary strengthening, the relationship of the yield strength σ_y (Using Tabor's relation σ_y=H/3) and strengthening mechanisms is expressed as:

$$\sigma_y=\sigma_0+\Delta\sigma_{ss}+\Delta\sigma_{gb}+\Delta\sigma_\rho+\Delta\sigma_{TW} \quad (2)$$

where σ_0 is the peierls stress for fcc Fe (112.5 MPa [51]), σ_{ss} is the solid solution strengthening, σ_{gb} is the grain boundary strengthening, σ_ρ is the dislocation strengthening, and σ_{TW} is the twinning boundary strengthening.

1.5.2.1 Solid solution strengthening

The solid solution strengthening $\Delta\sigma_{ss}$ is attributed by the substitutional atoms of Mn in the Fe lattice, which is expressed as [52]:

$$\Delta\sigma_{ss}=0.68*[70*(X^{at}_{MN})^{0.75}] \quad (1.3)$$

where X^{at}_{MN} is the concentration in wt% of element Mn, which is 0.3. As a result, $\Delta\sigma_{ss}$ is calculated as 19.3 MPa.

1.5.2.2 Grain boundary strengthening

$\Delta\sigma_{gb}$ is the strength caused by Hall-Petch strengthening, which can be calculated by the Hall-Petch equation [53]:

$$\Delta\sigma_{gb}=k_y*d^{-1/2} \quad (1.4)$$

where k_y is the Hall-Petch slope of bcc Fe (k_{HP}=0.357 MPa*$m^{1/2}$ in [54]), and d is the average width of the lamella structure (~200 nm). As a result, $\Delta\sigma_{gb}$ is calculated as 798.3 MPa.

1.5.2.3 Dislocation strengthening

$\Delta\sigma_\rho$ is the dislocation strengthening, and it can be calculated by the following equation [55]:

$$\Delta\sigma_\rho = M\alpha Gb\rho^{1/2} \quad (1.5)$$

where M is the Taylor factor, α is a correction factor specific to the material, G is the shear modulus, b is the Burgers vector, and ρ is dislocation density. Assume that the Fe-30wt%Mn in this study has similar parameters to the high-Mn steel (Fe-22Mn-0.6C in [52]), then M is 3, α is 0.3, G is 65 GPa, and b is 0.25 nm. The dislocation density of high-Mn steels processed by HPT ranges from $1.57*10^{15}/m^2$ to $1.76*10^{16}/m^2$ [49, 53]. In this study, assume that the dislocation density is $9.59*10^{15}/m^2$, the resultant dislocation strengthening is 1432.2 MPa.

1.5.2.4 Twin boundary strengthening

Deformation twining in high-Mn steels have been observed to alter the strength of the material [50]. The strengthening contribution of twin boundaries can be treated as Hall-Petch type strengthening, which can be estimated by the following equation [55]:

$$\Delta\sigma_{TW} = V_f * K_{TW} * l^{-0.5} \quad (1.6)$$

where K_{Tw} is a constant and can be approximated to that of a Hall-Petch constant of the nanocrystalline regime of a corresponding alloy ($k_{HP}=0.357MPa*m^{1/2}$ [54]) as the twin spacing (l) is in nm. V_f is the volume fraction of twins and it can be estimated by the following equation [53]:

$$\frac{1}{l} = \frac{Vf}{2e(1-Vf)} \quad (1.7)$$

where l is the spacing between twins and e is the twining thickness. From Figure 1.3 (c), l is estimated to be 94 nm while e is estimated to be 20 nm. As a result, the Vf is estimated to be 0.30. However, this equation assumes that twins exist all across the entire sample. In this study, it is observed that the Fe-30wt%Mn sample is composed of a lamella structure with two alternative phases – one is the austenite phase and another one is the martensite phase, as shown in Figure 1.3 (a). And the twining boundaries are only observed in the austenite phase. As a result, the real volume fraction F is assumed to be half of the calculated Vf, which is 0.15. Based on these parameters, $\Delta\sigma_{TW}$ is approximated to be 174.7 MPa.

1.5.3 The strength model of Fe-30wt%Mn processed by HPT

By using Eq. (2), the yield strength of Fe-30wt%Mn processed by 2 turns of HPT is assumed to be linearly contributed by each mechanism. Parameters in Eq. 2 are listed in Table 1.1, and the total yield strength is calculated to be 1937MPa by adding up the estimated magnitude of each strengthening mechanism. However, it is impossible that these strengthening mechanisms can work independently in the system. For example, the solute in the solid solution would act as obstacles for dislocation movement, resulting in a decrease of the average grain size. As shown in Figure 1.3, the dislocation walls would also break up initially large columnar grains and cause sub-grains, which form smaller grains in the end.

In addition, it is worth mentioning that the parameters are all estimated based on a series of assumptions. For example, it is assumed that all 30wt%Mn solute remains in the solid solution when calculating the solid solution strengthening. The grain size that is used to

calculate the grain boundary strengthening is not the true grain size, but the width of the lamella bands. The dislocation density is simply assumed based on other references. And the calculation of twin width and spacing can have errors.

As a result, the parameters of the strengthening mechanisms can only qualitatively indicate their contribution to the yield strength of Fe-30wt%Mn processed by 2 turns of HPT. As shown in Table 1.1, it can be observed that the dislocations play the most important role in strengthening the material. Grain boundaries and twin boundaries contribute to the total yield strength as well. The solid solution strengthening can be neglected in the system.

Table 1.1 Contribution of various strengthening mechanisms in Fe-30wt%Mn processed by 2 turns of HPT

σ_y	σ_0	$\Delta\sigma_{ss}$	$\Delta\sigma_{gb}$	$\Delta\sigma_{\rho}$	$\Delta\sigma_{TW}$
1937MPa	112.5MPa	19.3MPa	198.3MPa	1432.2MPa	174.7MPa

1.6 Conclusions

In this study, Fe-30wt%Mn samples deformed by HPT for one, two and four turns were investigated. Since the as-received Fe-30wt%Mn was too heterogeneous to be processed by HPT due to the large volume of dendrites, all samples were homogenized before HPT. The microhardness of homogenized Fe-30wt%Mn was relatively low due to columnar grains formed during homogenization (1100°C, 48h). After one turn of HPT, the microhardness increased significantly due to grain refinement and deformation twinning. However, the microhardness did not change significantly after two turns and four turns of HPT indicating dislocation saturation which caused suppression of nano-twinning,

dislocation-nanotwin annihilation, and unfavorable grain-orientation for easy slip. After several strengthening mechanisms are discussed, the grain refinement, high dislocation density and deformation twinning are considered dominant in the strengthening model of Fe-30wt%Mn after HPT.

Chapter 2. Surface Modification through Mechanical Alloying and Spark Plasma Sintering of Fe-30wt%Mn Alloys to Create Tailorable, Nano-porous, Bioresorbable Surfaces

2.1 Abstract

The effects and mechanisms of fabricating Fe-30wt%Mn by Spark Plasma Sintering (SPS) on its corrosion behavior have been investigated. The SPS process was applied to construct tailorable, nano-porous Fe-30wt%Mn to develop functional bioresorbable implants. The effects of SPS dwell time on the properties of synthesized Fe-30wt%Mn were studied. The results showed that nano-porous microstructure can be deliberately designed by making Fe-30wt%Mn via SPS. The resulting nano-sized structures have the potential to enhance initial cell attachment for future bioactive resorbable materials.

Keywords: Spark Plasma Sintering, bioresorbable, nano-porous

2.2 Introduction

Metals have been utilized as bio-implants over a hundred years thanks to the combination of their mechanical properties and bio-performance [56]. Unlike traditional corrosion resistant implants used clinically, those made by bioresorbable metals can be tailored to remain in the body for a specified amount of time, only to support the process of healing, after which the implants would generally degrade into non-toxic products and be replaced by tissues that grow back [57, 58]. In contrast, permanent implants would stay inside the human body as a foreign object, which would cause chronic risks, such as thrombosis and in-stent stenosis [59, 60]. Even if the corrosion resistant implant can be taken out after finishing its job, a second surgery would increase the risk of infection and damage to

surrounding areas, let alone pain and energy waste. Therefore, bioresorbable metallic materials, especially iron, magnesium and their alloys, are being broadly studied and modified when the whole healing process only requires contemporary implants [17, 61].

Both iron and magnesium have been tested as effective bioresorbable metals considering the safety, cell attachment and proliferation, and thrombogenicity [15, 62]. To get a better understanding of the corrosion rate of iron and magnesium, Pierson et al [63]. evaluated the bioresorbable behavior of iron wires and magnesium wires in rats and found that the corrosion rate of iron is too slow while the corrosion rate of magnesium is too fast compared to the time needed for tissue healing. For Fe, Peuster et al tested the long-term biocompatibility and claimed that the degradation rate of pure Fe should be increased [64]. For Mg, an additional fast degradation rate would cause a loss of necessary strength to support the whole healing process. Hermawan et al. did a comparison on mechanical properties of Fe and Mg alloy to SS316L, the most widely used alloy in all implants, and found that iron has closer mechanical properties to SS316L [65]. In addition, Waksma indicates that iron stents have a superior opportunity to be implanted compared with polymers and magnesium alloy because it is radio opaque [66]. Fortunately, alloying iron with manganese both decreases the thrombosis potential and increases the degradation rate [16]. In addition, Magnetic Resonance Imaging (MRI) uses magnets and radio waves to examine patients, which requires the implants to be non-magnetic. Youn et al. evaluated the manganese content on MRI susceptibility and recommended the Mn content to be more than 25wt% [67]. Hermawan et al made a comparison of mechanical strength and corrosion rate of Fe-Mn alloys with Mn content ranging from 20-35wt% and concluded that both Fe-

30wt%Mn and Fe-35wt%Mn are worth to be further studied for biomedical stents application [68].

However, bioresorbable implants are required to attain a controllable degradation rate, prolonged mechanical stability and excellent biocompatibility [69]. Besides, particles that are less than 3 μm pass through the lung to the liver and spleen while 10 μm particles get completely trapped in the lung [70]. Therefore, it is also necessary to refine the grain size of Fe-30wt%Mn to reduce the risk of blocked blood vessels.

Currently, one of the biggest issues in metallic resorbability is controlling the ever-changing interface between the degrading implant and growing new tissues as outlined by Zheng et al [71]. Upon implantation, chloride ions start breaking down the oxide layer over the entire exterior of the degradable metal, while proteins begin adsorbing to its surface, thereby affecting the rate of metallic dissolution [71]. In the case of bone fracture fixation devices, apatite is also deposited on these surfaces, while the filopodia of migrating cells sense the implant's surface irregularities, adhere, and multiply to construct healthy hard tissues [71, 72]. In addition, osteoblasts have been known to have a higher capacity to synthesize bone matrices on rougher surfaces [73]. Ryan et al. also mentioned that high surface area porous implants tend to show higher corrosion rates than non-porous implants [74]. Amidst all these complex interacting mechanisms, the dynamic resorbable interface needs to encourage tissue attachment, cell proliferation, and ingrowth to reduce chance of loosening or failure as it slowly disappears. However, little work has been conducted on SPS of resorbable biomaterials. The SPS process has the potential to enhance

tissue/implant interactions through drastically increasing surface area, roughness, and possibly degradability.

The purpose of present work is to better understand the fundamental mechanisms behind SPS Fe-30wt%Mn in order to generate tailorable surface porosities.

2.3 Materials and Methods

2.3.1 Sample Preparation

Commercial Fe powders with a purity of 99.8% and commercial Mn powders with a purity of 99.9% obtained from Atlantic Equipment Engineers company were used as the starting materials for mechanical alloying and subsequent consolidation. Both powders are at -325 mesh (<45 μm). Mechanical alloying was conducted using a SPEX 8000 mill obtained from SamplePrep company with a vial and 1/4-inch balls made of stainless steel (SS440). For each run, 50 g stainless balls, 7 g Fe powders, 3 g Mn powders and 0.1 g stearic acid were loaded into the stainless-steel vial inside a glovebox to prevent oxidation. The tightly sealed vial was then transferred out from the glovebox and installed in the SPEX 8000 shaker to go through a 10 min-on-5 min-off milling program with the milling time of 40h. Several runs were made to fabricate enough batches of alloyed Fe-30wt%Mn powder particles for the following consolidation process. The vial was then transferred back into the glovebox and the powder particles that were smaller than 45μm after milling were sieved with a 325-mesh sieve to be loaded into a 15 mm SPS die. SPS was then used as the consolidation process to form bulk Fe-30wt%Mn disks. The chamber of SPS was vacuumed and pumped with argon for three times to insure an argon atmosphere during SPS. Three of them were used in the corrosion test while another sample was used as a

comparison for that in a pre-corrosion condition. The thickness of each sample is around 1 mm.

2.3.2 Materials Characterization

All samples were mechanically ground to 1200 grit, polished with alumina and colloidal silica, rinsed with isopropanol and air dried before they were chemically etched via Nital solution (2% HNO_3 in methanol). Visible-light microscopy was performed to examine the microstructures after each processing step and SEM (Nova NanoSEM 450) equipped with concentric backscattered detector (CBS) and Energy Dispersive Spectroscopy (EDS) was used to examine the microstructure of Fe-30wt%Mn samples. Transmission Electron Microscopy (TEM FEI Tecnai12) was utilized to observe the microstructure of Fe-30wt%Mn after HPT. The TEM sample was prepared with Focused Ion Beam (FIB, Scanning DualBeam Microscope Quanta 3D 200i). XRD was used to study the phases and grain size of samples. Williamson-Hall [25] was used to measure grain size of Fe-30wt%Mn by a software called HighScore. Density of the Fe30wt%Mn samples made by SPS were measured according to Archimedes' principle as described in the ASTM B962-13 standard.

2.3.3 Mechanical testing

Vickers Hardness for materials were measured using Micro Vickers Hardness Tester (Phase II, model no.900-391) equipped with optical microscope, under 1 kg f load with dwelling time of 15s. 14 measurements were recorded for each sample and the distance between each indent is 1mm.

2.3.4 Static Immersion Test

Disk specimens (d = 15 mm, t = 1 mm) were ground, polished, cleaned (described in Section 2.2) and weighed before exposure to the corrosion media. Three samples were tested for each material. The samples were immersed in Kokubo's solution for 504 h (21 days) at T=37 ℃ and pH=7.40. The simulated body fluid is prepared based on Kokubo's paper [75]. The pH of the testing solution was checked every three days during the test. A slight increase of pH was observed so the solution was replenished every three days to maintain the pH during the immersion period. After the test, the specimens were cleaned by the cleaning solution. The cleaning solution was made by dissolving 3.5g hexamethylenetetramine in 500mL hydrochloric acid (HCl, sp gr 1.19) and adding water up to 1000mL. The samples were cleaned ultrasonically in the solution for 5 min at room temperature, rinsed with deionized water and finally dried and stored in a desiccator for 24h before weighing. The corrosion rate was calculated according to the following equation [76]:

$$CR = \frac{K \times W}{A \times T \times D} \tag{2.1}$$

Where CR is the corrosion rate in millimeters per year (mmpy), W is weight loss (g), A is area (cm^2), T is time of exposure (h), D is density (g/cm^3).

2.4 Results and Discussion

As shown in Figure 2.1, there are obviously higher martensite ε peak intensities in group 3, especially at the angle around 45° and 59°, which shows martensitic transformation in group 3. Therefore, it is assumed that immersing Fe-30wt%Mn samples at 900 ℃ for a longer time during SPS would result in martensitic transformation and therefore increase

hardness. Moreover, Williamson-Hall [77] was used to measure grain size of Fe-30wt%Mn by a software called HighScore. The calculated grain sizes are 9.2 nm, 186 nm, 58 nm and 34 nm for Fe-30wt%Mn SPEX milled powders with group 1, 2 and 3, respectively. Although some errors are inevitable during calculations, such as the machine errors or the process of measurement, it provides a general idea that grain growth obviously occurred during SPS and grain size of Fe-30wt%Mn decreases from group 1 to group 3. The microstructural refinement from group 1 to group 3 can be explained by recrystallization of austenite, enhancing martensite formation from milling-deformed austenite during cooling process of SPS from 900 ℃ to room temperature. Meanwhile, the fast heating and cooling rate in SPS prohibited grain growth of obtained martensite plates. Kanetsuki et al. observed fine ferrite-pearlite microstructure transformed from fine dynamic-recrystallized austenite grain without coarsening of post dynamically recrystallized fine austenite grains by controlling the cooling rate to 10 ℃/s immediately after controlled rolling [78]. The lamellar spacing of pearlite can be refined down to 50nm by conventional heat treatment [79]. It is known that martensite has a fine structure even in its original state [80], meaning that martensitic transformation alone would result in grain refinement.

Table 2.1 shows the densities of Fe-30wt%Mn in group 1, 2 and 3 before the static immersion test. The densities of different groups are pretty much the same, which excludes the effects of density on the microhardness results. The initial microhardness of the alloys before static immersion test is shown in Figure 2.2. The possible explanation for the highest hardness of group 3 can be martensitic transformation that occurred at high temperatures as a heat treatment process. In detail, SPEX milling processes pure Fe and pure Mn

powders to be synthesized into austenite Fe-30wt%Mn alloys as a severe plastic deformation. The state of austenite is very unstable thermally and undergoes a partial martensitic transformation at certain temperatures [81]. Dr. Stancia investigated martensitic transformation of Fe-Mn alloys via heat treatment, which is reflected as hardness increase of the material [76]. Since the martensite phase has relatively higher hardness and density compared to the austenite phase, it has a strengthening effect in the structure of alloys [82, 83].

Table 2. 1 Densities of Fe30wt%Mn in group 1, 2 and 3.

Group	Density (%)	SD
1	0.952	0.014
2	0.954	0.002
3	0.95	0.005

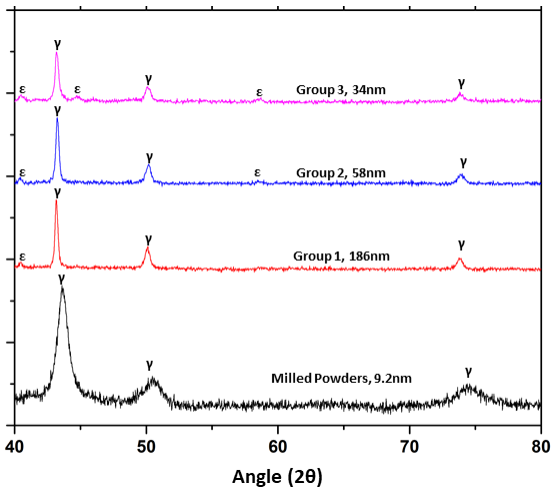

Figure 2.1 X-ray pattern of Fe-30wt%Mn before and after SPS.

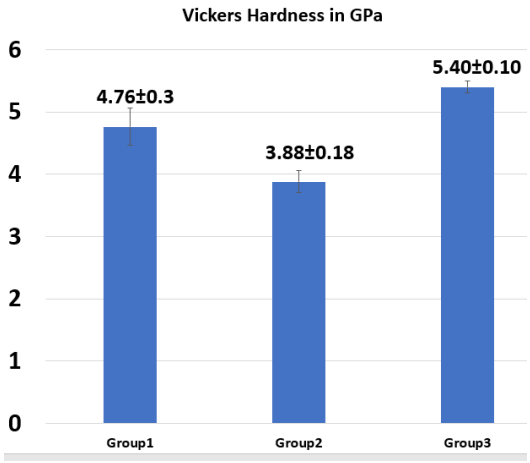

Figure 2. 2 Vickers hardness of Fe-30wt%Mn alloys in group 1, 2 and 3 before static immersion test.

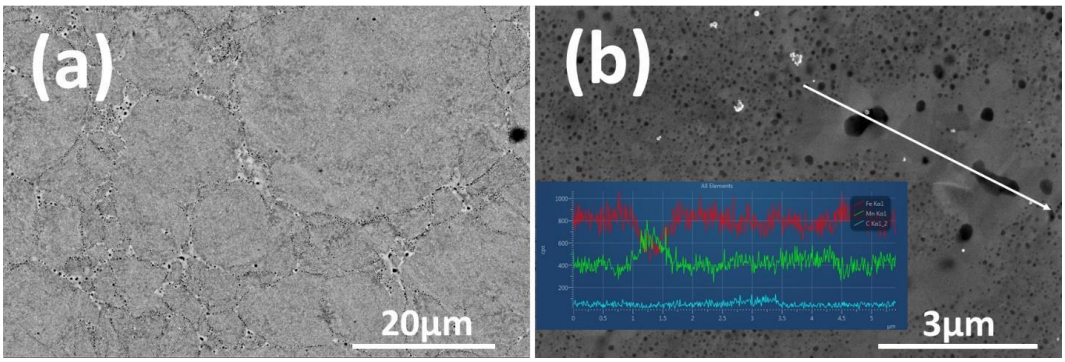

Figure 2.3 Microstructure of Fe-30wt%Mn before static immersion test (a), an enlarged area with two larger pores and its corresponding EDS line analysis (b).

Figure 2.3 (a) shows microstructure of Fe-30wt%Mn before static immersion test. It is observed that regions between initial particles are occupied with pores. Figure 2.3 (b) shows an enlarged area with two larger pores and its corresponding EDS line analysis. The area within the initial particle is also porous. But those pores are tiny and pores between initial particles are relatively larger. In addition, the corresponding EDS line analysis on two larger pores shows that those pores are Mn-rich areas, resulting from diffusion of Mn atoms to the surface area which contains higher free energy. Theoretically, Mn is less noble

than Fe [84], and the Mn-rich region is supposed to degrade faster. Experimentally, Lia Stanciu et al. have confirmed that the Mn-rich area in Fe-Mn alloys is more susceptible during degradation. Therefore, it is predicted that the pores would be expanded as the Mn-rich area is degraded during static immersion test.

Figure 2.4 (a) shows microstructure of Fe-30wt%Mn in group 1 after static immersion test. It is noticed that there are some colonies with more materials left while the region between colonies is corroded more. Those colonies should be initial particles and the area between initial particles is degrading faster. Figure 2.4 (b) shows microstructure of Fe-30wt%Mn in group 2 after static immersion test. It is observed that Fe-30wt%Mn in group 2 is degraded more uniformly. Figure 2.4 (c) shows microstructure of Fe-30wt%Mn in group 3 after static immersion test. More obvious localized corrosion is observed, resulting from a more bioactive martensite phase, and the remaining sites represent a cupped microstructure. Figure 2.4 (d) shows an enlarged area of Fe-30wt%Mn in group 2 after a static immersion test. The corroded material is still full of tiny pores, which correspond to those tiny pores within initial particles. These microstructures confirm the assumption that pores, especially larger pores, are degrading faster considering that those pores are Mn-rich areas. The uniform degradation can be explained by uniform porosity of Fe-30wt%Mn in group 2. Vandrovcova et al. suggests that irregularities less than 100 nm emulate the size of adhesion receptors on cells and moreover interact well with adsorbed cell adhesion [85]. Murphy et al. also suggests that small pores may be beneficial for initial cell adhesion, whereas large pores improve cellular infiltration [86]. After dealloying, it was additionally observed that the grain boundaries were preferentially etched and a variety of other larger

pores developed on the exterior at arbitrary intervals, possibly due to localized etching at defect sites [10].

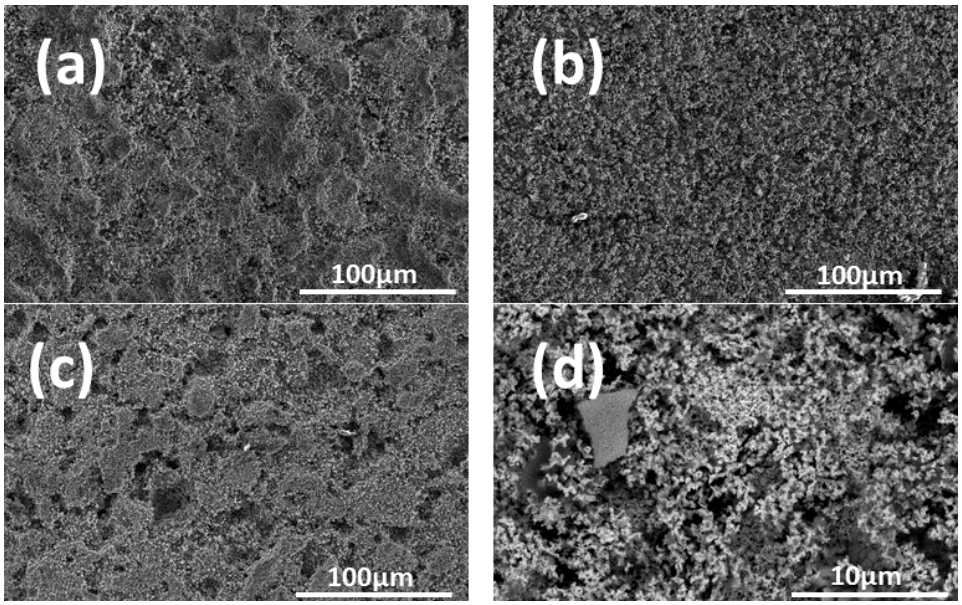

Figure 2.4 Microstructure of Fe-30wt%Mn in group 1 (a), group 2 (b), group 3 (c) and an enlarged area of Fe-30wt%Mn in group 2 (d) after static immersion test.

Table 2.2 shows the calculated corrosion rate of Fe-30wt%Mn in group 1, 2 and 3 after 21 days of static immersion test. It is noted that the corrosion rate for each group is almost the same except that Fe-30wt%Mn in group 2 degrades a little bit faster than that in another two groups. The higher corrosion rate of Fe-30wt%Mn in group 2 can be explained by a more uniform porosity. Instead of being attacked with some preferential region, Fe-30wt%Mn in group 2 is attacked more uniformly, which means the attacked area is relatively larger against another two groups. Stanciu et al. synthesized two Fe-30wt%Mn alloys by sintering Mn with different initial Fe powder size and measured their corrosion rate. The calculated corrosion rate was 1.36 mmpy for samples made by coarse-grained

(30-200 μm) Fe and 0.29 mmpy made by fine-grained Fe (<44 μm) [76]. It seems that the corrosion rate of Fe-30wt%Mn is within this range.

Table 2.2 Calculated corrosion rate of Fe-30wt%Mn in group 1, 2 and 3 after 21 days of static immersion test.

Group	Corrosion Rate/mmpy
1	0.34 ± 0.02
2	0.39 ± 0.03
3	0.34 ± 0.05

2.5 Conclusions

In this study, Fe-30wt%Mn was fabricated by mechanical alloying and consolidated by SPS with three different programs. The microstructures of Fe-30wt%Mn alloys before and after the static immersion test were studied. It appears that Fe-30wt%Mn alloys processed by SPEX mill and SPS are full of tiny porous while the region between initial milled particles is occupied with relatively larger pores. These pores acted as the vulnerable area during static immersion tests and degraded faster than other areas. In addition, Fe-30wt%Mn in group 2 obtains the most uniform microstructure, which enhances corrosion rate. It is concluded that with a well-designed mechanical alloying process and SPS program, a nano-porous, tailorable bioresorbable Fe-30wt%Mn can be achieved.

Chapter 3: Microstructure and mechanical response of bulk nanocrystalline Cu-Ta alloys consolidated by Spark Plasma Sintering

3.1 Abstract

Nanocrystalline (NC) Cu-Ta alloys (Cu-1, 3, 5 & 10Ta, at%) have been investigated as high-strength NC materials partially due to their relatively stable microstructures against grain growth. Such microstructurally stable Cu-Ta alloys are mostly fabricated by cryomilling and consolidated by Equal Channel Angular Extrusion (ECAE). Spark Plasma Sintering (SPS), in contrast, provides an alternative approach to consolidate the Cu-Ta alloys by providing a rapid rate. Cu-10at%Ta made by SPS exhibits a smaller average grain size and similar microhardness with that made by ECAE at the same temperature. Several strengthening mechanisms in the Cu-Ta alloys are discussed to conclude the predominant strengthening mechanisms: Hall-Petch effect, rule-of mixture strengthening and Zener pinning. These strengthening mechanisms combined with various processing conditions explain the different microstructures and mechanical properties of Cu-10at%Ta consolidated by SPS and ECAE. Finally, it is concluded that SPS should be used when a small sample is needed in a faster and easier way, while ECAE is recommended when a relatively large sample with higher strength is required.

Keywords: cryomilling, Spark Plasma Sintering, consolidation

3.2 Introduction

There has been growing research interest in nanocrystalline (NC) materials due to their superior strength properties compared to their coarse-grained counterparts [20]. However, most NC materials suffer deleterious grain growth [21]. caused by diffusional creep, grain

boundary sliding and rotation, at low homologous temperatures or under mechanical loads which drive stress-driven grain growth. These thermal and mechanical limitation continue to present challenges to the application of NC alloys in applied conditions, such as the aerospace, naval, civilian infrastructure and energy sectors [22].

Methods to circumvent these concerns have, to some extent been researched in both experimental work and computational simulations. In particular, it has been shown that certain immiscible systems, such as Cu-Ta, can retain NC grains under elevated temperature and mechanical loading conditions, and in doing so, the high-strength properties are retained [87-89]. The stability, however, is maintained via both solutes in a supersaturate state and <5 nm solute clusters, and the lack of miscibility makes attaining these microstructural features requires processing techniques that drive non-equilibrium states. In immiscible materials systems such as Cu-Ta, this can be achieved by cryomilling, a simple and inexpensive technique involving repetitive fracturing and cold welding of powder particles at cryogenic temperature (-197℃). During cryogenic processing, the ductile and soft Cu powder particles are more susceptible to deformation and cold welding rather than fracturing in the initial milling process while the Ta powder particles are brittle (the ductile-to-brittle transition temperature is -200℃). Therefore, the Ta powder particles are more likely to fracture and tend to comminute, while the Cu powder particles, as they continue to cold weld, tend to increase in size. The small, fractured Ta particles then tend to become trapped in the cold welded Cu particles as milling continues. Both the presence of trapped fine Ta particles and the severe plastic deformation caused by ball collisions are responsible for the grain refinement to the nanoscale in the Cu matrix. With further milling,

the ductile Cu particles work-hardened and begin to fracture into smaller particles and continued to mix with Ta particles. Lastly, the blended powder particles experience repetitive fracturing and cold welding, resulting in a supersaturated Cu-Ta solid solution. Using this method, NC Cu-10at%Ta that has been shown to maintain a mean grain size of 167nm after annealing at 97% of the melting point of Cu and exhibits nearly twice of the microhardness of conventional pure Cu, which is attributed to the kinetic pinning effect of Ta nanoclusters at grain boundaries [24]. Moreover, such NC Cu-Ta alloys have shown to possess excellent high-temperature creep resistance, with a creep rate 6-8 orders of magnitude lower than that of a typical NC metals [23].

After cryomilling the Cu-Ta particles often need to be consolidated into fully dense bulk (cm-scale in one dimension) structures for further testing. The spark plasma sintering (SPS) [90, 91] and equal channel angular extrusion (ECAE)[92, 93] methods have the ability to bond and densify the milled powders with minimal grain growth and thus retention of strength properties. In the ECAE method, the powders are encapsulated in cored-out billets which are electron-beam welded under inert atmosphere, and then processed via elevated temperature severe plastic deformation, which can be multipass, however, the simultaneous imposition of shear and pressure often result in full density after one ECAE pass. As an alternative consolidation approach, SPS is a novel sintering technique which facilitates rapid heating rate by pulsed current joule heating to sinter the compacted powders into a bulk sample at a relatively low temperatures in a much shorter sintering time compared with other conventional sintering processes [94]. These conditions facilitate the sintering of nanograined Cu-Ta particles with limited grain growth.

While the studies implementing ECAE to consolidate mechanically alloyed Cu-Ta powders into a fully dense NC samples are plentiful,[95-97] there are much less reports on usage of the SPS method. A preliminary report implemented both SPS and ECAE independently, but with the same precursor powders, however the microstructural evolution and mechanical response of the SPS consolidated materials are not reported, nor are the mechanisms that may control the resulting strength.[89] A more recent report by Rahmanifard et al. studied high-energy planetary milling (non-cryogenic) combined with either vacuum hot-pressing or SPS at varied Ta loading contents and temperatures on the electrical and mechanical properties of dilute Cu-Ta alloys [98]. In their study, the extent of Ta solubility and crystallize size are presented, along with the bulk density achieved post-SPS and the resulting hardness and electrical conductivity, however data on only one SPS processing condition (Cu-5at%Ta + 850°C for 2 min at 30 MPa pressure) is given, and even under these conditions, full-density is not achieved.

The present study is aimed at further explore the possibility of using SPS to consolidate thermally stable alloys, but through careful consideration of process parameters to achieve full density. Once this is achieved, microstructural and mechanical probes will be performed to understand the contributions of the diverse resulting microstructural features on the hardness. In this way, the microstructure, thermal stability and mechanical behavior of NC Cu-Ta alloys (Cu-1, 3, 5 & 10Ta, at%) fabricated by cryomilling and subsequent SPS can be better understood. Scanning Electron Microscopy (SEM), Transmission Electron Microscopy (TEM), and high-resolution TEM (HRTEM) are utilized to observe the surface microstructures, grain size and grain size distribution of Cu grains and Ta

segregations. Post-SPS consolidation, Vickers hardness testing and static compression tests are applied to study the mechanical behavior of the fabricated Cu-Ta alloys. This study shows that although the refined Cu grain size grows slightly after SPS, they are still nanoscale in dimensionality (<100 nm) which further validates the well-studied thermal stability of the Cu-Ta system, but under SPS consolidation conditions. Several theorized strengthening mechanisms are discussed to explain the enhanced mechanical properties. Finally, the microstructures and mechanical properties of Cu-10at%Ta made by SPS and ECAE are compared to analyze the varying effects of consolidation via these two distinct methods. These findings forecast the ability for alternative consolidation approaches for the manufacture of bulk, nanocrystalline components with stability against detrimental grain growth and property losses.

3.3 Materials and Methods

3.3.1 Sample Preparation

3.3.1.1 Cryomilling

Commercially pure Cu powder (99.9%, -100 mesh) and Ta powder (99.9%, -325 mesh) (both from Atlantic Equipment Engineers Co., Upper Saddle River, New Jersey, USA) were used as the starting materials for high energy cryogenic mechanical alloying (MA). For each run, 50 g of nominally 12.5 mm diameter (0.5 inch in diameter) tungsten carbide (WC) balls, 10 g Cu and Ta powders with varying mass based on intended composition (Cu-1, 3, 5,10Ta, at%) were loaded into SPEX 8004SS steel-jacketed WC grinding vial. Sample loading was performed in a high-purity Ar glovebox to minimize oxidation and contamination. The tightly sealed vial was then transferred from the glovebox and installed

in a modified SPEX 8000D Dual Mixer/Mill (Metuchen, New Jersey, USA) device. A custom modification was made to allow the vial to be surrounded with a thick polymeric sleeve and feeding system containing liquid nitrogen (LN), thereby facilitating sustained cryogenic temperatures during milling. Each powder run was cryomilled for 4h without interruptions. After milling, the vials were transferred back to the glovebox and the alloyed powders were sieved with a 140-mesh sieve to obtain particle sizes smaller than ~105μm for the SPS consolidation process. Several runs were made to synthesize enough batches of alloyed Cu-Ta powders for bulk sample densification in the SPS.

3.3.1.2 Consolidation Process – SPS

An annular graphite SPS die with a 10 mm inner diameter bore was lined with a 0.5mm thick graphite foil and transferred into the Ar glovebox. The foil is used to prevent direct contact of the powders with the graphite die. Approximately 1.5 g of the Cu-Ta powders was loaded inside the die cavity between two ~10mm diameter cylindrical punches. Graphite foils were also placed between the punches and the powders to prevent direct contact of the powders and the punches. The die set-up was then transferred from the glovebox and placed inside the SPS device (Fuji Dr. Sinter Lab Jr.). The chamber was vented and evacuated three times to remove residual air and maintain vacuum. The sample processing cycle consisted of subjecting the powder to an axial pressure of 75 MPa, ramping at 75 ℃/min to a temperature of 900 ℃, dwelling at 900 ℃ for 20 min, and then sample cooling at a rate of 75 ℃/min as well. The die assembly was extracted, and the consolidated Cu-Ta alloy was ultrasonically cleaned, ground with SiC paper from 600 to

1200 grit and then polished with alumina and colloidal silica. Full densities (> 99%) of these final bulk products were verified using the Archimedes method [99].

3.3.1.3 Microstructural Characterization

Both the as-cryomilled Cu-Ta powder alloys and bulk alloys produced by SPS were characterized by XRD (PANalytical Empyrean Series 2) using a Cu-K x-ray source over a 2-theta angle from 30° to 100°. The largest Cu peak (111) was used with the Scherrer equation [8] to estimate the crystal size of Cu-Ta alloys before and after SPS. The grain size estimation obtained via the Scherrer equation presents a useful, albeit qualitative analysis as instrumental broadening effect masks the peak sharpening effect of grain growth. Scanning electron microscopy (SEM) (ThermoFisher Scientific NNS450*)* was used to observe the surface microstructures of the SPS processed alloys while transmission electron microscopy (TEM) (ThermoFisher Scientific Tecnai 12) was used to observe the grain structure and grain size distribution of the Cu grains and Ta segregants. Scanning transmission electron microscopy (STEM) (ThermoFisher Scientific Titan Themis 300) was used to observe the Ta nanoclusters which were smaller than 20 nm in diameter and to probe the coherence with the Cu lattice. Foils with a thickness of 50-70 nm were prepared by Focused Ion Beam (FIB) (ThermoFisher Scientific Quanta 3D 200i) for TEM and STEM analyses.

3.3.1.4 Mechanical Testing

The microhardness of SPS processed alloys was measured by Vickers micro-indentation (Phase II, Model No. 900-391 Series) with a load of 9.8N and a dwell time of 15 s. For each sample, 15 indents were applied, and the average hardness was calculated. A 3 mm

diameter × 3 mm height cylinder was prepared to undergo quasi-static compression testing using an electro-mechanical load frame with an initial strain rate of 0.01 s^{-1}.

3.4 Results

The cryomilling and SPS processing used for this study results in fully dense (>99%) NC Cu-Ta alloys with each of the desired compositions (Cu-1, 3, 5,10Ta, at%). Figure 3.1 (a) shows a bright-field TEM image of the Cu-10at%Ta made by SPS. Both the Cu grains and a large density of Ta segregations with random orientations are observed. These grains appear to have low dislocation densities and well-defined grain boundaries suggesting the presence of a large fraction of high angle grain boundaries at the grain interfaces. There is a large distribution in the size of the Ta segregants, and the sizes of those smaller than 30 nm are difficult to resolve from Figure 3.1 (a). Therefore, Figure 3.1 (b) presents a STEM image of Ta segregants smaller than 30nm. The colored arrows (see online version of manuscript for color image) indicate the nominal size of different coherent or semi-coherent segregations (blue, ~1 nm; red, ~2.5 nm; yellow, ~4 nm or greater). Similar Ta features are also observed in Cu-Ta alloys made by mechanical alloying plus ECAE consolidation [24]. In this study, Ta segregants larger than 30 nm are called Ta particles, while those smaller than 30 nm are called Ta nanoclusters, although there is no clear dividing line to distinguish them. Figure 3.1 (c) and (d) give the corresponding grain size histograms of Ta particles and Ta nanoclusters, respectively. The grain/particle size are measured using the linear intercept method with ImageJ software. Based on Figure 3.1 (a) and (c), the average Cu crystallite size is approximated to be ~110 nm and the mean size of Ta particles is approximated as ~90 nm. From Figure 3.1 (b) and (d), the mean size of

the Ta nanoclusters is ~4 nm. In addition, the size of the Ta segregants exhibits a bimodal distribution. In Figure 3.1 (c) and (d), the size of the Ta particles is within the range of 30-150 nm, while the size of Ta nanoclusters is predominantly smaller than ~15 nm. This bimodality of Ta segregant distribution results in multiple strengthening mechanisms, which will be discussed in more detail in later sections. Moreover, the Ta nanoclusters near grain boundaries tend to be larger than those residing inside the Cu grains, which is likely a result of the higher diffusion rate of Ta atoms along grain boundaries in contrast to the grain interior grain interior [100].

Using the Scherrer equation [37], the largest Cu peak (111) was used to estimate the crystallite size before and after the SPS processing. The grain size of Cu-Ta alloys grows from ~20nm to ~45nm after the 20 min of SPS process at 900℃. As a comparison, the grain size of pure nanocrystalline Cu consolidated by SPS has been reported to increase from 50nm to 260nm when the temperature reaches 500℃.[101] Fig. 2 shows the XRD peaks of the cryomilled powders and SPS processed bulk materials for Cu-10at%Ta and detail the Cu(111) peak changes and shifts as a result of the SPS processing. The Cu (111) peak sharpening likely indicates grain growth of Cu grains during SPS. In addition, the Cu (111) peak shifts to a higher angle after SPS, suggesting some Ta decomposition from the supersaturated Cu-Ta solid solution attained during the cryomilling.

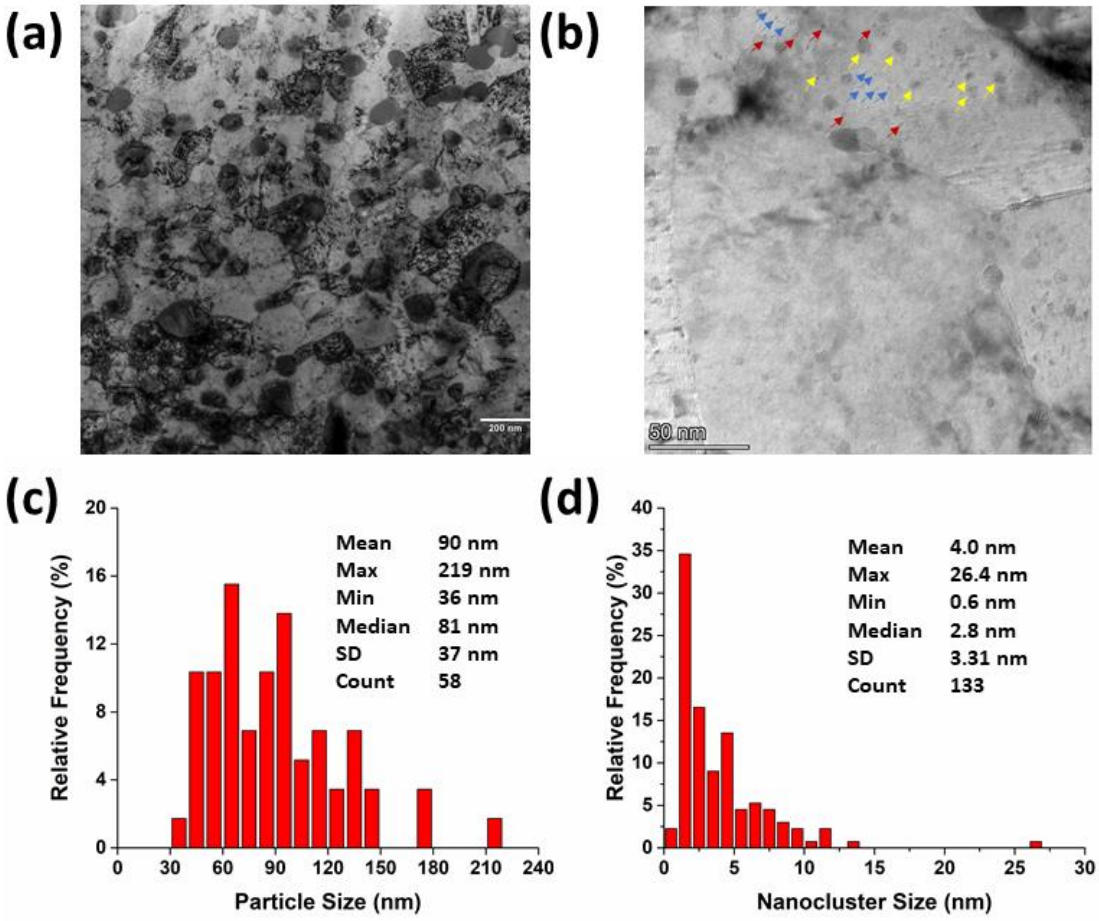

Figure 3.1 (a) and (b) Bright-field TEM images of the Cu-10at%Ta made by SPS processing; the colored arrows indicate the sizes (radius) of the different coherent or semi-coherent nanoclusters (blue, approximately 1 nm; red, approximately, 2.5 nm; yellow, 4 nm or greater); (c) Ta particle size (>30 nm) histogram; and (d) Ta nanocluster size (<30 nm) histogram of Cu-10at%Ta made by SPS. Color figures are available in the digital online version of this manuscript.

In general, the Vickers hardness of the SPS processed Cu-Ta alloys is harder than NC Cu and also increases as the Ta content is increased as shown in Fig. 3. The measured values are consistent with the microhardness analysis of Cu-Ta alloys made by ECAE consolidation, where Cu-10at%Ta has a higher Vickers harness than that of Cu-1at%Ta [97]. As would be expected, the microhardness of the SPS processed Cu-10at%Ta is more

than that of pure coarse-grained copper consolidated by SPS [101] and nanocrystalline Cu with comparable grain sizes [102]. In the current study, Cu-5at%Ta demonstrates the highest microhardness among the alloy compositions tested. This may be a result of excess contamination during the cryomilling process. Contaminants such as oxygen and WC can come from multiple sources, and have also been reported in a prior similar SPS study [98]. where impurities of oxide and carbide compounds are shown. Minor impurity levels may enhance grain size stability and microhardness through grain boundary pinning effects [103], which act similarly with the Zener pinning effect via Ta nanoclusters. With the stochastic nature of ball-milling, it is reasonable to believe that some WC contamination is induced, which may increase the hardness of materials in this study, but within a certain range of hardness values. A plausible reason is that as the Ta content increases, the system reaches a point where the Ta solute is supersaturated to a maximum extent, and therefore further solid-solution hardening is limited. This circumstance can be inferred from the data showing that the hardness of the Cu-5at% and Cu-10at%Ta are within a standard deviation of each other, as shown in Figure 3.3.

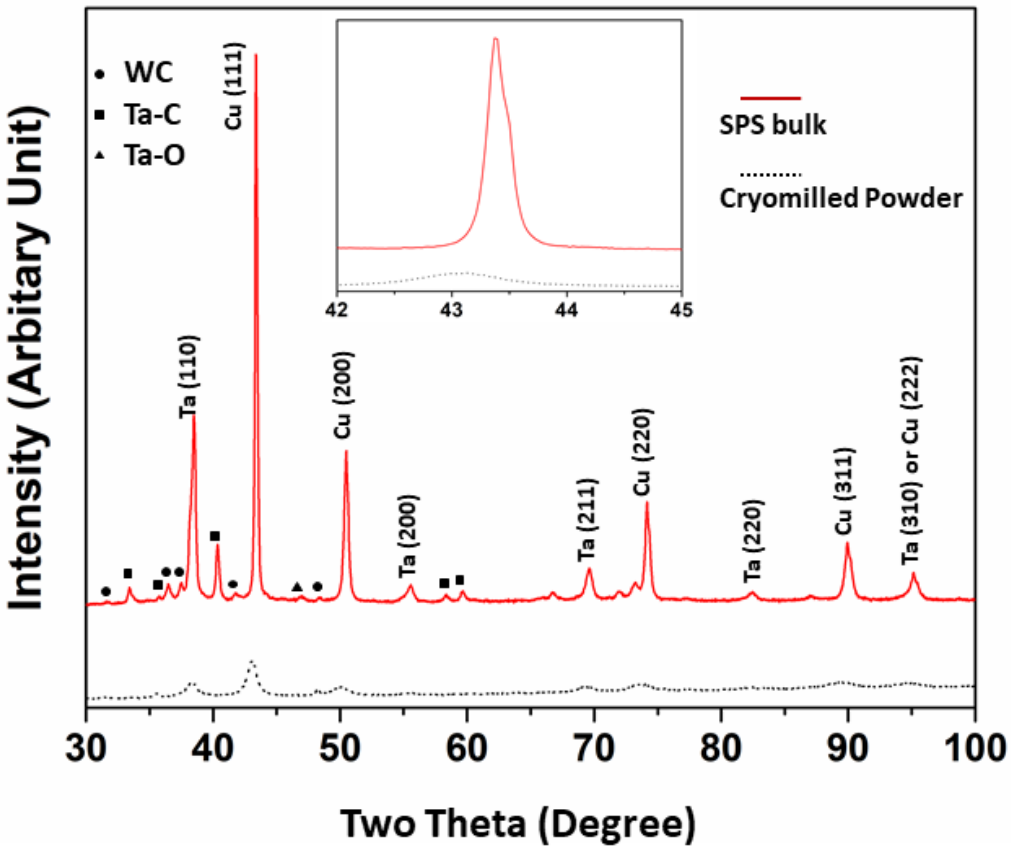

Figure 3.2 XRD of cryomilled powder and SPS bulk for the Cu-10at%Ta composition. The image shows details of the Cu (111) peak changes and shifting.

To compare the compression mechanical response with literature reports on ECAE consolidate Cu-10at% material [104], a single uniaxial compression test was performed on the NC Cu-10at%Ta made by SPS. As shown in Figure 3.4, the compressive stress-strain curve of the Cu-10at%Ta made by SPS exhibits near elastic-perfectly plastic behavior with no substantial strain hardening. In addition, the fracture strain of this alloy is approximately 0.2, which is very close to that of the Cu-10at%Ta made by ECAE tested at the same strain rate [104]. The NC Cu-10at%Ta made by SPS also displays a 0.2% offset compressive yield strength of ~735 MPa, which is lower than that of the ECAE counterpart (1100 MPa), but more than twice of that of a pure NC Cu with a comparable grain size (110 nm, 300

MPa) [102]. This enhanced yield strength of the Cu-10at%Ta is attributed to a few predominant strengthening mechanisms including grain size strengthening (the so-called Hall-Petch effect), rule-of-mixture strengthening, and Zener pinning by Ta nanoclusters at the Cu grain boundaries, which will be discussed.

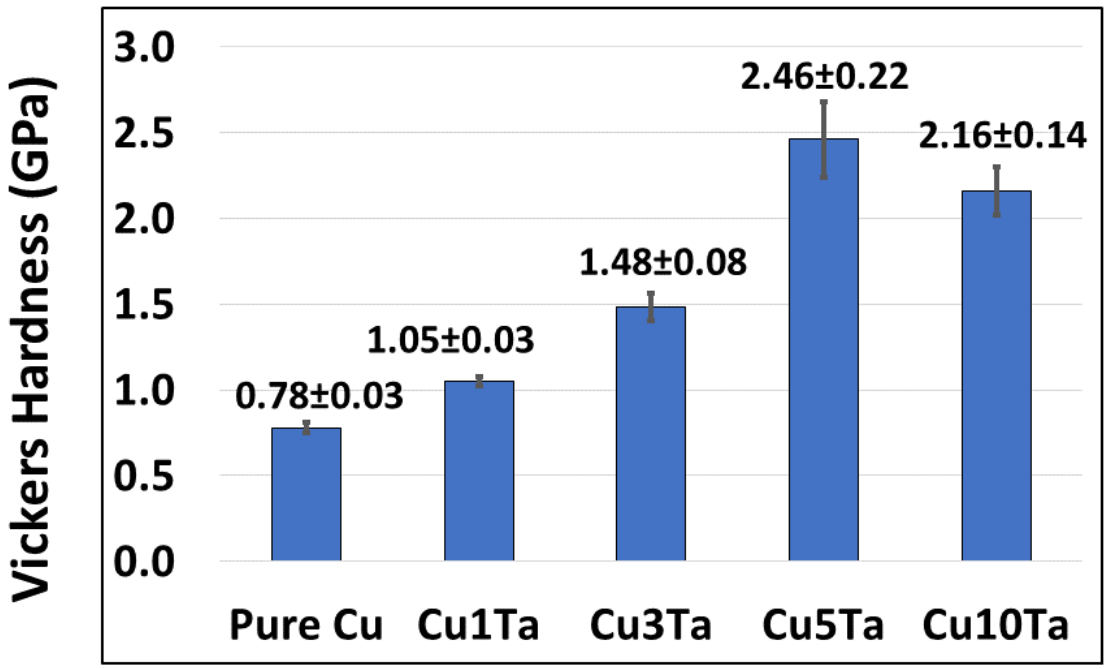

Figure 3.3 Vickers microhardness of pure Cu and Cu-Ta alloys (Cu-1, 3, 5 & 10Ta, at%) made by SPS processing.

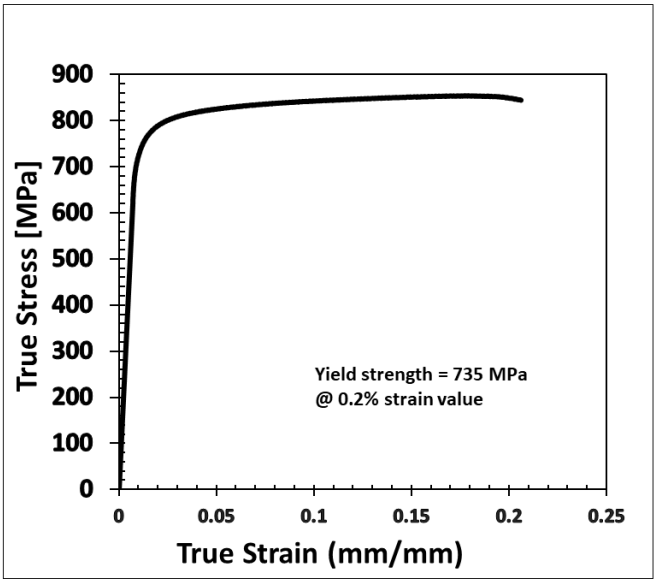

Figure 3.4 Uniaxial compression mechanical response of the SPS processed NC Cu-10at%Ta at a strain rate of 0.01 s−1 .

Table 3.1 Thermomechanical processing conditions of three different Cu-Ta processes: ECAE [97], and SPS

Processing conditions	Temperature	Time	Applied load	Rate of deformation	Grain size for Cu-10at%Ta	Microhardness for Cu-10at%Ta
ECAE	700 ℃	40 min	compression and shear	Higher	70 nm	3.75 GPa
	900 ℃				213 nm	2.12 GPa
SPS	900 ℃	40 min	**Uniaxial Compression**	**Lower**	**110 nm**	**2.16 GPa**

3.5 Discussion

3.5.1 Mechanisms contributing to strengthening

Fully dense NC Cu-Ta alloys with grain size stability at elevated temperatures have been successfully fabricated by cryomilling and SPS consolidation. Figure 3.1 shows the bimodality of Ta segregants, which are divided into Ta particles (> 30 nm) and Ta nanoclusters (< 30 nm). Rajagopalan et al. also parsed the Ta particles and clusters based on size, and additionally calculated the coherency of Ta nanoclusters with the Cu matrix based on their interfacial energy. They report the Ta nanoclusters to be coherent, semi-coherent, and incoherent based on their sizes of < 3.898, from 3.898 nm to 15.592 nm, and > 15.592, respectively [95]. Another assumption based on size was reported by Darling et al. who suggested that particles below a critical diameter of 30 nm can no longer be sheared by dislocations [97]. These findings suggest that Ta particles are predominantly incoherent and Ta nanoclusters are predominantly coherent or semi-coherent. This bimodality of Ta additions, combined with the solid solution and grain size reduction contributions suggests several different strengthening mechanisms in the Cu-Ta systems, as discussed below.

3.5.2 Solid solution strengthening

While supersaturated Cu-Ta solid solution can be achieved by cryomilling, elevated temperature consolidation causes the Ta solutes to segregate out of the matrix and form Ta nanoclusters; these then serve as non-shearable barriers to dislocation movement, stabilize the grain boundaries and thus contribute to the strengthening [105]. In the present study, this decomposition process occurs during the SPS processing. The binary equilibrium

phase diagram for Cu-Ta suggests complete separation of Cu and Ta atoms at the SPS processing temperature of 900 ℃, however, due to the slow diffusion of Ta in the Cu lattice [100] and the short time of the SPS process (20 min at the 900℃ temperature), the decomposition process can only occur to a limited degree. Some small fraction of the Ta solute may remain in solid solution in the Cu matrix after SPS. To estimate the Ta content in supersaturated solid solution after SPS processing, the lattice parameter of the consolidated Cu-10at%Ta $a_{Cu\text{-}Ta}$ is approximated from the angle of the Cu (111) peak (2θ = 43.3691°) using Bragg's law and Vegard's law, and is found to be 0.36094 nm. The solubility of Ta is then calculated via a rule-of-mixture equation:

$$a_{Cu\text{-}Ta}=a_{Cu}(1-x)+a_{Ta}x \tag{3.1}$$

where *a* is the lattice parameter, and *x* is the Ta content in solid solution. Based on Eq. (1), taking the lattice parameter values of Cu and Ta to be 0.36146 nm and 0.33030 nm, respectively [106], Ta content in solid solution *x* is calculated to be 1.7%. Using the same method, Darling et al. calculated that approximately 2at%Ta was forced into the Cu lattice in a Cu-10at%Ta alloyed that had been cryomilled for 4h, but prior to ECAE consolidation [24]. During high-temperature annealing at 600ºC for 10min, it was reported that the Cu–Ta alloys undergo phase separation of the as-milled forced solid solution and grain growth of the resultant nucleating phases [107]. Atom probe tomography mapping indicates that a significant volume fraction of Ta atomic clusters result from this decomposition process [105]. In the present study, this decomposition process occurs during SPS, but to a lesser extent. It can be inferred that the short time of exposure during SPS is insufficient to cause all of the Ta solutes to precipitate out of the lattice into Ta nanoclusters, and some solid

solution strengthening may still occur. With regards to the strengthening potential of solutes versus nanocluster, Koju et al. simulated GB motion in a random solid solution and compared the results with a Zener pinning of grain boundaries in Cu-Ta alloys [108] Their results show that while both strengthening mechanisms reduce the grain boundary mobility, the effect of solid solution strengthening is not as potent as in the presence of Ta clusters on dislocation trapping [108].

3.5.3 Orowan strengthening

Another potential contributor to strengthening in the resultant microstructure is Orowan strengthening, wherein dislocations bow around particles in the matrix. Darling et al. suggested that this component of strengthening occurs when incoherent Ta particles larger than 30 nm reside at the Cu lattice [97]. In the current study, the microstructures in Figure 3.2 indicate that many Ta particles have diameters comparable to the Cu grain size, and they do not reside in a Cu lattice. Moreover, if Orowan strengthening was prevalent, the accumulation of dislocation loops around particles would dramatically enhance the strain hardening. However, the true stress-true strain compression plot given in Figure 3.4 shows nearly elastic-perfectly plastic behavior with no substantial strain hardening in the Cu-10at%Ta SPS processed alloy. Therefore, Orowan strengthening is not considered to be a predominant strengthening mechanism in the SPS processed Cu-Ta materials.

3.5.4 Hall-Petch effect (grain size strengthening)

Within grain size ranges greater than 10s of nm, the strengthening increase due to reduction in grain size can be estimated using the empirical Hall-Petch equation:

$\sigma_y = \sigma_0 + kd^{-1/2}$

(3.2)

where σ_0 is 25.5 MPa, and k is reported to be 0.11 MN/m$^{3/2}$ for pure Cu [109].

In the present study, the average grain size of Cu in the SPS processed Cu-10at%Ta is ~110 nm. From Eq. (2), the approximated yield strength σ_y is 360 MPa. Using Tabor's relation ($H=3\sigma_y$), this corresponds to a hardness increment of 1.08 GPa in pure Cu. The total hardness measured for this composition is 2.16 GPa, indicating that the Hall-Petch effect only partially contributes to the strengthening observed.

3.5.5 Rule-of-mixture hardening (Ta particles)

The large Ta particles that are comparable in size (90 nm) to the grains of the Cu matrix (110 nm) may possibly contribute to rule-of-mixtures strengthening. According to Atwater et al [110]., the relationship between hardening from the role of mixtures (H_{rom}) and hardening from the Hall-Petch effect (grain size reduction) (H_{HP}) is:

$H_{rom}=f(H_{Ta}- H_{HP})$

(3.3)

where f is the volume fraction of Ta and H_{Ta} is the hardness of pure Ta. As already presented, H_{HP} is approximated to be 1.08 GPa. For the Cu-10at%Ta alloy, the volume fraction of Cu (f_{Cu}) is estimated to be 85.8% and the volume fraction of Ta (f_{Ta}) is 14.2% based on their atomic radii (Cu 128 pm, Ta 146 pm) and the overall composition. Literature reports the Hall-Petch parameters of Ta to be σ_0 = 78.45 MPa, and k = 0.4 MN/m$^{3/2}$ [109]. With these assumptions in place, the yield strength (σ_y) of pure Ta with a grain size of 90 nm should be ~1.41 GPa. Using Tabor's relationship ($H=3\sigma_y$), the hardness of pure Ta with

the grain size of 90 nm is 4.23 GPa. This result is in a good experimental agreement with the previous report on the hardness of pure Ta in a similar grain size [111]. Based on Eq. (3), the resultant H_{rom} is 0.45 GPa, which suggests a relative contribution to the total strength of ~ 21%.

3.5.6 Zener pinning at grain boundaries

The Ta nanoclusters at grain boundaries come from cryomilling and decomposition of Ta solutes from previous supersaturated Cu-Ta alloys. The function of Ta nanoclusters at the Cu grain boundaries can be explained by Zener pinning [108, 112, 113]. The large pinning stress by the Ta nanoclusters and the quantitative agreement with the Zener pinning model provide strong evidence that the high-temperature stability of the Cu-Ta alloys is attributed by the Zener pinning effect [108]. Zener pinning effects can also explain the possible reason why the Vickers hardness of Cu-5at% is the highest among all NC Cu-Ta alloys (Cu-1, 3, 5 & 10Ta, at%), as shown in Figure 3.3. The Zener pinning equation is [112]:

$$Pz = \frac{3F\gamma}{2r} \tag{3.4}$$

where Pz is the Zener pinning force due to all particles on a grain boundary, F is the volume fraction of the particles, γ is the energy per unit area of a grain boundary (surface tension of a grain boundary, J/m^2), and r is the particle radius. Obviously, more nanoclusters with smaller radius would result in larger pinning pressure. As the Ta content increases, on the one hand, higher volume fraction (F) would occur, which would add in the Zener pinning effect; but on the other hand, too much Ta elements would result in larger radius (r) because of the limited solubility in the immiscible Cu-Ta system, which would instead decrease the

Zener pinning effect. It is reasonable to believe that there is a balance when the microhardness reaches a maximum point closer to 5at%.

3.5.7 Precipitation strengthening in the grain interior

As shown in Figure 3.2 (b), most Ta nanoclusters observed at the Cu grain boundaries are relatively larger than those observed in the grain interior, caused by higher diffusion rate of Ta atoms at grain boundaries than that inside the Cu grains [100]. The Ta nanoclusters in the grain interior result from the decomposition of previous supersaturated solid solution [108], which is confirmed by Cu (111) peak shifting to higher angle after SPS, as shown in Figure 3.2 (b). Similar results have been observed in another immiscible alloy system – Cu-Nb alloys, in which almost all Nb atoms diffused out from supersaturated Cu-Nb solid solution after annealing at 400, resulting in a decrease of microhardness [114]. The difference is that the Nb was observed to form nanoscale precipitates inside the Cu grain, while Ta was observed to segregate along grain boundaries more than that in the grain interior. The decreased microhardness caused by the decomposition of Nb atoms indicates that the precipitation strengthening in the grain interior is not even stronger than the solid solution strengthening. The decomposed Ta nanoclusters in the grain interior are supposed to pin the individual dislocations inside the Cu grains and prevent the growth of sub-grains. However, Figure 3.1 shows very limited dislocations and sub-grains in the grain interior of Cu-10at%Ta, indicating that the precipitation strengthening by Ta nanoclusters in the grain interior does not contribute enough to the overall strength. To compare the strengthening mechanisms of two models of Ta nanoclusters, Frolov et al. simulated two different distributions of Ta atoms in Cu and concluded that Ta segregation at the Cu grain

boundaries increases the microstructural stability and mechanical strength compared with a uniform distribution of the same amount of Ta [45]. Therefore, the segregation strengthening of these Ta nanoclusters in the grain interior is not considered one of the predominant strengthening mechanisms.

3.5.8 Predominant mechanisms occurred in this study

Based on the discussions above, the predominant strengthening mechanisms in the SPS Cu-Ta alloys include the Hall-Petch effect, rule-of-mixture strengthening, and the Zener pinning effect, which interact with each other. For instance, the Zener pinning effect of Ta nanoclusters reduces the average grain size of the Cu matrix by preventing the movement of grain boundary, which contributes to the Hall-Petch effect. In addition, the rule-of-mixture strengthening is affected by the Hall-Petch strengthening, as indicated in Eq. 3. As a result, although Hall-Petch strengthening contributes to 50% of the total strength and rule-of-mixture contributes to 21% of the total strength, the Zener pinning effect contributes to more than 29% of the total strength.

Although the estimated share of contribution for each strengthening mechanism is only qualitatively, it helps our understanding of microstructural and mechanical response of the Cu-Ta system fabricated by cryomilling and SPS.

3.5.9 Thermomechanical processing condition effects on the microstructural and mechanical response

Thermo-mechanically stable immiscible Cu-Ta alloys can be fabricated by various processing methods, of which the processing conditions affect the deformation mechanisms, thereafter the microstructural and mechanical response of the final products.

In this session, three bottom-up processing methods: (1) cryomilling + SPS, (2) cryomilling + ECAE, and (3) sputter deposition are discussed and compared to enhance our understanding of the Cu-Ta system.

In this study, concerning the Cu-Ta alloys fabricated by cryomilling and SPS, the strengthening mechanisms are controlled by two parts. For the first part, cryomilling, high energy ball mill at a cryogenic temperature was used to mechanically force the Ta atoms to be incorporated into the Cu lattice, thus achieving an extended Cu-Ta solid solution. This kinetic approach refined the microstructure of the material, which enhanced the Hall-Petch effect and rule-of-mixture strengthening. In addition, the Ta atoms forced into the Cu lattice enhanced solid solution strengthening, while forming nanoclusters at the Cu grain boundaries enhanced Zener pinning effect. For the second part, SPS with a uniaxial pressure was applied to consolidate the cryomilled Cu-Ta powders into a bulk sample, during which microstructure coarsening and thermal decomposition occurs. Considering microstructure coarsening, Lu et al. have studied the grain growth and strain release in NC Cu and found that the grain growth process is dominated by grain boundary diffusion [60]. In detail, the residual strain caused by cryomilling is rereleased during SPS. In the meantime, the self-diffusion of Cu atoms is activated by the high temperature caused by Joule heat; the atoms diffuse into voids at grain boundaries and drive grain coarsening, which reduces Hall-Petch strengthening. Competitively, Ta atoms decompose from previous supersaturated solid solution and form Ta nanoclusters at the Cu grain boundaries, which is called thermal decomposition in this study. The coherent and/or semi-coherent nanoclusters at grain boundaries act as barriers to prevent grain coarsening, which enhances

the Zener pinning effect. Also, the inhibition of grain coarsening significantly enhances the mechanical properties of Cu-Ta alloys due to the Hall-Petch effect, which shows that finer grains exhibit a higher hardness.

For the Cu-Ta alloys fabricated by cryomilling and ECAE, the consolidation process is different from that in this study. Table 3.1 shows various processing conditions of cryomilling + ECAE [42] and cryomilling + SPS, including temperature, time, the form of applied load, and the rate of deformation. These processing conditions guide the deformation and mechanisms in the material, resulting in corresponding microstructural and mechanical response of the material.

As shown in Table 3.1, the grain size of Cu-10at%Ta made by SPS is smaller than that made by ECAE at 900 ℃, which can be explained by three plausible reasons. The first reason can be that SPS takes less time than ECAE for the Cu grain coarsening since the self-diffusion rate of Cu atoms increases as the time and temperature increase [115, 116]. The second reason is that the volumetric heating caused by the Joule effect during SPS is different from the conductive heating in conventional sintering systems. In detail, current and Joule heat are focused at the neck formed between the Cu-Ta powder particles, resulting in a gradient temperature from the contact interfaces and the center of the particles. Such a gradient temperature can confine the diffusion of Cu and Ta atoms in the inner region of the particle, resulting in a smaller grain size of the Cu-Ta alloys made by SPS than that made by ECAE at the same setup temperature. The last reason is that ECAE applies a severe shear strain on the sample which shears Cu grains and Ta particles into a smaller size, while SPS just applies a static 75 MPa pressure on the powder particles. Zhang

et al. have shown that the initial pressure and the holding pressure used in the SPS process only have a slight influence on the microstructures and mechanical properties of Cu compared with the sintering temperature [101]. In contrast, the extrusion of ECAE was repeated four times, resulting in a total strain of ~450% [105]. Such severe strain applied by ECAE results in severe plastic deformation of the sample, causing dislocation activities. Evidence has shown that the high dislocation density, generated in pure Cu by ECAE, breaks down original grains and forms sub-grains/cells, resulting in a grain refinement [40, 117].

As for the mechanical response of Cu-Ta alloys affected by deformation/strengthening mechanisms, Table 3.1 shows that although Cu-10at%Ta made by ECAE has a larger grain size than that made by SPS both at 900 °C, their microhardness is almost the same, indicating that Hall-Petch and rule-of-mixture, which are highly affected by grain size, are not the only predominant strengthening mechanisms. Indeed, the Zener pinning effect by Ta nanoclusters at the grain boundaries is of great importance in enhancing the mechanical strength of the sample. As discussed in 3.5.6, the Zener pinning equation [112] shows that the Zener pinning force can be increased by the total amount of Ta nanoclusters at grain boundaries. The longer processing time of ECAE would cause a higher amount of Ta nanoclusters decomposed from the solid solution than that made by SPS, resulting in a stronger Zener pinning force at grain boundaries. Therefore, the microhardness of Cu-10at%Ta made by ECAE and SPS obtain the same microhardness even though the ECAE sample has larger grain size than that made by SPS. As shown in Figure 3.4, NC Cu-10at%Ta made by SPS displays the yield strength of about 735 MPa at 0.2% strain value,

which is smaller than that of Cu-10at%Ta made by ECAE (1100 MPa) tested at the same strain rate [104]. The lower yield strength of NC Cu-10at%Ta made by SPS is partially caused by the Hall-Petch effect since the average grain size of the SPS sample is 110 nm and the ECAE sample is 50 nm. And the discussed higher Zener pinning force in the ECAE sample adds up to the yield strength of the material. In addition, experiments have shown that the enhanced strength of Cu during plastic deformation is attributed by the dislocation activity rather than grain boundary sliding [118]. The famous Taylor equation [119] and Nix-Gao equation [120] have quantitatively shown that the strength of a material is increased by the increase of the dislocation density. The details of these equations are not discussed here because the strengthening mechanisms in Cu-Ta alloys are much more complicated than their assumed situation. Nonetheless, the high dislocation density is considered responsible for the fact that SPS sample obtain a similar microhardness with the ECAE sample even though the ECAE sample has a larger grain size and that SPS samples exhibits a lower yield strength than ECAE sample processed at the same strain rate.

Unlike SPS and ECAE, the processing conditions of sputter deposition is much less limited. For instance, co-deposited Cu-Ta nanocomposites can be fabricated at various temperatures ranging from -120 °C to 800 ℃, resulting in corresponding microstructures [121, 122] In addition, the time needed for sputter deposition is much more flexible than SPS and ECAE, depending on the deposition rate and the total thickness of the final products [25, 107]. As a result, the deformation and strengthening mechanisms of the deposited Cu-Ta alloys can be different. For example, Wang et al., observed that the shear

banding deformation of deposited Cu-Ta thin films are layer thickness dependent [123]. Given the stochastic nature of the ball mill, the extended Cu-Ta solid solution can vary from run to run, while sputter deposition can be highly controlled and deterministic. In this study, Ta solute in the SPS Cu-Ta solid solution is calculated to be 1.7%. Similarly, previous reports have demonstrated up to 2at%Ta in a supersaturated solid solution in the ECAE samples [24, 88]. However, up to 10at%Ta content in the solid solution has been observed in Cu-Ta system made by sputter deposition [124]. These results indicate that more Ta can be dispersed into the Cu-Ta solid solution by sputter deposition than SPS and ECAE. While thermomechanical stability of Cu-Ta system of the SPS sample in this study is achieved by the Zener pinning effect of Ta nanoclusters at the Cu grain boundaries, the layered structure in the deposited Cu-Ta thin films prohibited recrystallization and grain growth of the Cu-rich phase by placing diffusion barriers of Ta-rich phase within the sample. Moreover, while in this study cryomilling induces residual strain in the Cu-Ta alloys, the heating and cooling during deposition induces internal stress caused by the coefficient of thermal expansion mismatch of the Cu and Ta.

3.6 Conclusions

Microstructural stability and mechanical strengthening of NC Cu-Ta alloys (Cu-1, 3, 5 & 10Ta, at%) made by SPS are investigated in this study. It is suggested that the predominant strengthening mechanisms are Hall-Petch effect, Rule-of-mixture strengthening and Zener pinning. Solid solution strengthening and segregation strengthening are possibly occurring in the Cu-Ta system, but they are not considered predominant. Cu-10at%Ta made by SPS and ECAE are compared to analyze the optimum consolidation process for immiscible Cu-

Ta system. As a result, if only a small sample is needed for basic microstructural analysis, such as SEM and TEM, SPS is suggested to save the sample and the work. On the contrary, if a relatively large sample is needed for mechanical testing, which requires a certain geometry of the sample, ECAE is recommended in this case. Moreover, ECAE is suggested when the strength of Cu-Ta alloys needs to be as high as possible. The present study shows that SPS consolidation of Cu-Ta powder particles enhances the design of bulk NC alloys for extreme-condition applications**.**

Chapter 4. Decoupling of Strain and Temperature Effects on Microstructural Evolution during High Shear Strain Deformation

4.1 Abstract

The interplay between defect generation by shear strain and defect annihilation by local heating is difficult to predict in shear assisted processing techniques. In this study we decoupled the effects of high shear strain and external heating in an immiscible Cu-Nb alloy using a pin-on-disk tribometer to mimic the microstructural evolution of material during solid phase processing. The change in sub-surface deformation, strain distribution and redistribution of second phase as a function of temperature were examined using transmission electron microscopy and atom probe tomography. Comparisons with a bulk scale process were made by quantifying the deformation using Zener-Hollomon parameter.

Key words: shear strain deformation, forced mixing, phase transformation, solid state processing, tribology

4.2 Introduction

Solid phase processing (SPP) of immiscible alloys involving high shear strain and processing-generated heat results in peculiar microstructures and outstanding properties of materials [26-28]. Generally, severe shear deformation during SPP of metals and alloys, results in microstructural refinement assisted by grain rotation [29], dislocation assisted plastic deformation [30], self-organization of second phase [31], and often shear induced atomic mixing [32, 33]. In contrast to microstructural refinement, grain growth has also been observed in some SPP cases, such as that in the weld zone during stir friction processing [34]. The microstructural coarsening is usually contributed by severe shear

generated thermal activation, which could directly impact the transformation pathways during deformation. While SPP is widely used for advanced material manufacturing and processing, the effects of strain and local heating due to process remain implicit. For example, during friction stir processing (FSP), the dissipation of heat is sluggish, and the processing temperature is often > 200 ºC [35]. Hence, the interplay between the defects' generation by shear processing and their annihilation by increased temperature is difficult to predict and understand.

To decouple the effects of shear strain and temperature, we used a pin-on-disk tribometer to mimic subsurface microstructural changes in a Cu-Nb binary system under shearing at various temperatures. The idea is that the tribometer process does not generate as much heat as SPP when the load and speed is under control. For instance, extensive dynamic recrystallization was detected in pure Cu under high load (10N) dry sliding wear, but not observed in low load (1N) dry sliding wear [125]. In this case, while Cu-4at%Nb alloy is subjected to a high strain cyclic shear deformation, the two-phase immiscible system undergoes a severe shear deformation below a tribometer wear track resulting in a highly refined microstructure at high strain. Afterwards, external heating (200 ºC and 400 ºC) is applied during the tribological process to elucidate the coupled effects of shear and temperature. The thickness of Nb particles is used to estimate the phase specific strain accommodation as a function of total strain and temperature. As a result, the influence of external heating can be studied on the severe shear deformation and dynamic recrystallization of a Cu-Nb immiscible alloy.

4.3 Materials and Methods

The binary Cu-4 at% Nb alloy was cast and remelted five times for homogenization. Samples with dimensions of 20 mm × 10 mm × 3 mm were cut using a slow speed saw, mechanically ground to 2000 grit, and metallographically polished using a 0.02 μm colloidal silica solution. Dry sliding and reciprocating wear tests were performed on the as-cast alloys using RTEC universal tribometer with temperature control with an active feedback loop to heat the stage up to 400 ℃. A 6.35 mm diameter stainless-steel ball was used as a counterface. Tests were conducted in ambient air (~32% RH) under a normal load of 1 N. The sliding frequency was set to 20 Hz for all the tests which were equivalent to a sliding velocity of 0.2 m/s. Wear tests were run for a total time of 20 min with 7 mm stroke length corresponding to 140 m of sliding distance to study steady-state friction behavior. Sliding and reciprocating tests were done at RT, 200 ℃, and 400 ℃. The temperature was held constant for at least 30 min prior to the wear tests. MFT17 software was used to record the coefficient of friction (CoF) and the wear tracks were analyzed using white light interferometry (WLI) at 10X magnification. 3D profiles of the wear tracks were stitched and analyzed to calculate the wear volume loss (mm^3) using Gwyddion software. Wear rates (mm^3/N.m) were calculated by dividing wear volume loss with load and the sliding distance. At least three tests were carried out at each temperature and the average value was reported. Cross-sectional wear tracks were characterized using scanning electron microscopy (SEM), backscattered electron diffraction (BSED), electron backscatter diffraction (EBSD), bright-field transmission electron microscopy (BFTEM), high-resolution transmission electron microscopy (HRTEM), selected area diffraction

patterns (SADP), and atom probe tomography (APT). The sample preparation of HRTEM and APT was performed using a Thermo Fisher Scientific Quanta 200 FIB-SEM outfitted with an Oxford Instruments X-ray Energy Dispersive Spectroscopy (EDS) system for compositional analysis. A FEI Titan 80–300 operated at 300 kV was used for HRTEM. A CAMECA LEAP 4000X HR APT was used in pulsed voltage mode at a 200 KHz pulse frequency with 20% pulse fraction, a specimen temperature of 50–60 K, and a detection rate that was maintained at 0.005 atoms/pulse.

4.4 Results and Discussion

The SEM micrograph in Figure 4.1 (a) has the bright contrast particles distributed throughout the matrix, which are highlighted by blue color in the corresponding Nb EDS map (Figure 4.1 (c)) while the gray matrix is Cu enriched (Figure 4.1 (b)). The average size of the Nb rich particles is measured to be ~ 1.7 μm. No compositional partitioning of Cu in the Nb rich phase (or vice versa) is observed in the as-cast condition. The structure of the two phases is consistently indexed as body centered cubic (BCC) for Nb and face centered cubic (FCC) for Cu as shown in Figure 1 (d) where (d1) and (d2) have the SADP collected from [100] Cu and [113] Nb. The tribometer is used on the surface of this sample and the resultant CoF and wear rate as a function of sliding temperature (RT, 200 ℃, 400 ℃) is shown in Figure 4.1 (e), more details on the friction and depth profiling about the wear test are given in *supplementary Figure S1*. In Figure 4.1 (e), there is an increase in CoF from 0.49 ± 0.05 to 0.80 ± 0.05 and an increase in wear rate from 0.2 ± 0.05 to 0.65 ± 0.07 (10^{-4} mm^3/N.m) with the increase in temperature from RT to 400 ℃. The increase in the CoF at elevated temperature can be explained by formation of hard Cu oxide particles

that are either thrown away or act as a third body participating in aggressive wear, which are shown using TEM in our post examination of subsurface sheared region presented later in the paper.

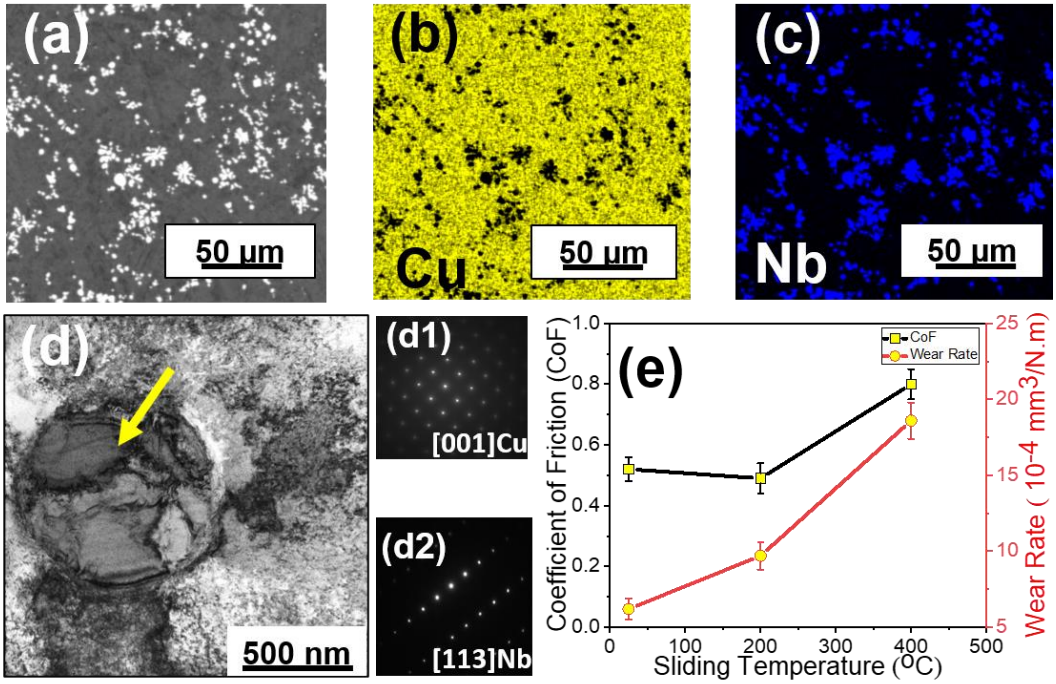

Figure 4.1 (a) SEM image of as-cast Cu-4at%Nb, (b) EDS map of Cu element, (c) EDS map of Nb element, (d) a spherical Nb particle pointed by a yellow arrow in the Cu matrix, (d1) diffraction pattern showing that Cu is FCC, (d2) diffraction pattern showing that Nb is BCC, (c) CoF and wear rate as a function of sliding temperature.

The tribological responses of the as-cast Cu-4at%Nb alloys processed at various temperatures are significantly related to their subsurface microstructures. As shown in Figure 4.2, EBSD images of Cu-4at%Nb processed by the pin-on-disk tribometer at (a) RT, (b) 200 ºC, and (c) 400 ºC indicate a general increase of grain size beneath the track as the temperature increases. Figure 4.2 (d), (e) and (f) show the corresponding misorientation plots as a function of distance. The relative flat regimes in Figure 4.2 (f) denote grain relaxation and growth at 400 ºC, which is not obvious in Figure 4.2 (d) and (e). As a result,

the EBSD indicates more pronounced dynamic recrystallization of Cu grains at 400 °C. This result corresponds to the observation that more material removed in Cu-4at%Nb processed at a higher temperature (*supplementary Figure S1*) because the subsurface material gets softer due to a larger average grain size. In addition, the EBSD line-scan analysis for the RT and 200 ºC sample in Figure 4.2 (b) and (e) indicates plastic deformation of the sample up to 30-40 µm below the surface followed by gradual grain rotation; while in Figure 4.2 (f) for the sample processed at 400 ºC, the plastic deformation regime extended to 135 µm below the wear surface. Previous studies have shown that CoF in alloys increases when the deformed zone thickness increases [126, 127]. These observations are consistent with our result that the CoF of the sample processed at 200 °C (0.49 ± 0.05) is lower than that processed at 400 °C (0.80 ± 0.05), as shown in Figure 4.1 (e). Finally, it is worth mentioning that although grain growth and recrystallization occurred at both 200 °C and 400 °C, the Cu grains are still much refined by the cyclic shear induced via the tribometer test compared with the original as-cast condition (Figure 4. (a)). It is well accepted that elevated temperatures have a deleterious effect on the mechanical strength of Cu [128], while Nb maintains its mechanical strength during annealing until 600 ºC [85]. As a result, the reduced thickness of the initially spherical Nb particles can be considered as a function of shear strain, and the response of Nb particles to elevated temperatures can be negligible. In addition, both Cu and Nb are ductile. Therefore, the extend of deformation for Nb particles can be used to calculate the local strain according to Dauzenberg and Zaat [129]:

$$\varepsilon = \left[\frac{D^2/c^2 - 1}{3}\right]^{1/2}$$

(4.1)

where ε is the strain applied on each Nb particle, D is the initial spherical Nb particle size, and c is the thickness of the sheared Nb particle. Figure 4.3 (a) shows one example of reduced Nb particle thickness as it gets strained when moving closer to the sample surface. Based on the morphology of the sheared Nb particles *(supplementary Figure S2)*, shear strain induced in Cu-4at%Nb samples at different temperatures, on tribological subsurface shear deformation, as a function of distance to the sample surface is plotted in Figure 4.3 (b). For Cu-4at%Nb processed at RT, the maximum strain near the surface was estimated to ~200 which resulted in formation of <5 nm thick Nb filaments [130]. The fact that at a similar depth, the sample processed at a higher temperature undergoes a lower shear strain is explained by two competing mechanisms: thermally activated process and shear-driven forced mixing [131]. At relatively low temperatures, the shear-driven forced mixing would be more dominant and achieve a highly refined microstructure; while at elevated temperatures, thermally driven diffusion of atoms would be enhanced and form coarser microstructures, such as mesoscopic patterning, and reprecipitation and redistribution of deformed Nb particles [131].

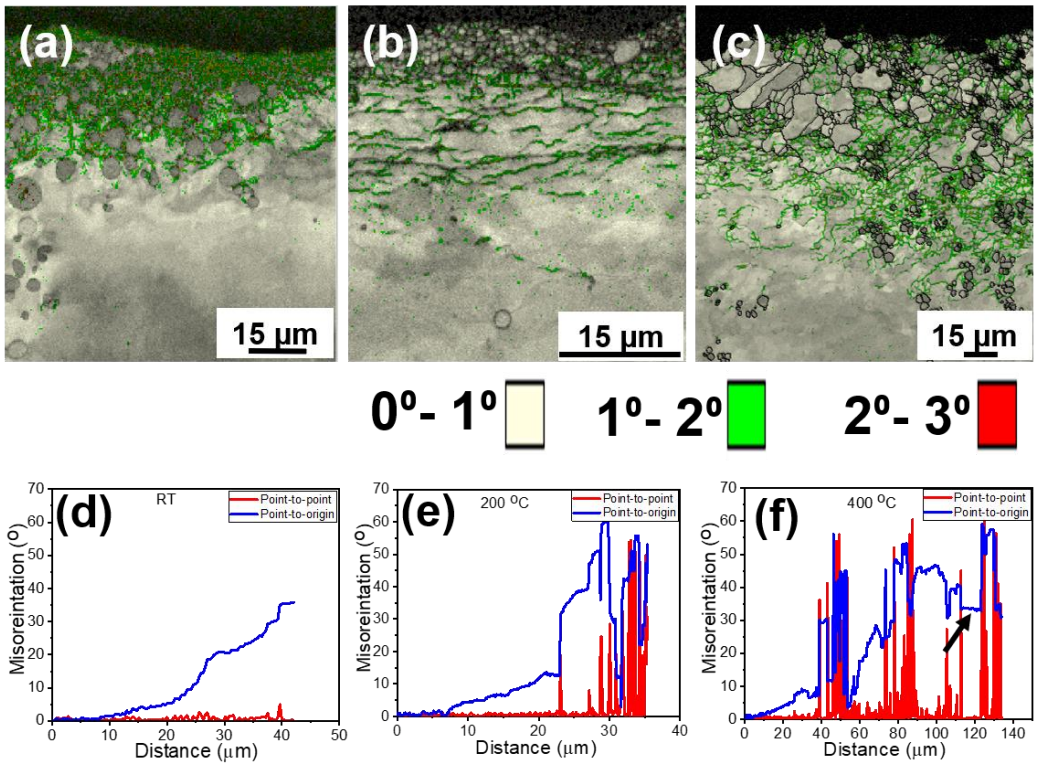

Figure 4.2 EBSD images of Cu-4at%Nb processed by the pin-on-disk tribometer at (a) RT, (b) 200 ºC, and (c) 400 ºC; and corresponding misorientation plots as a function of distance at (d) RT, 200 ºC, and (f) 400 ºC with a relative flat region (pointed by a black arrow).

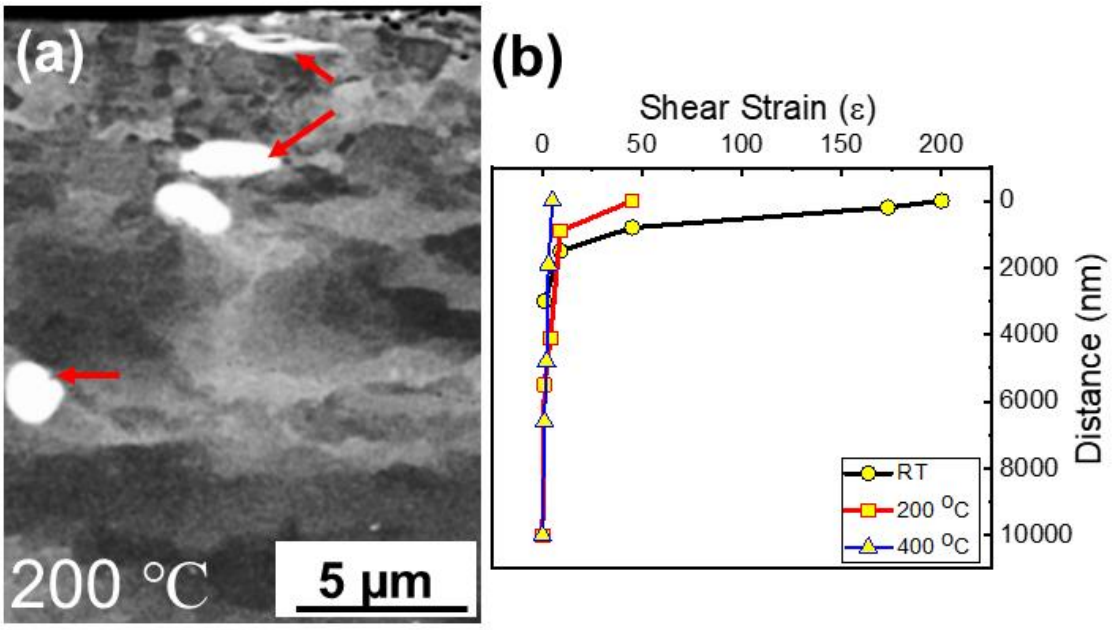

Figure 4.3 (a) SEM image of Cu-4at%Nb processed at 200 ºC showing decreased Nb particle thicknesses as a function of depth. (b) Estimated shear strain applied on Cu-4at%Nb samples as a function of distance to the sample surface.

Figure 4.4 (a) shows the subsurface microstructure of Cu-4at%Nb processed at RT by tribometer, where a gentle transition from the nanocrystalline (NC) region to the ultra-fine-grained (UFG) region as a function of depth and plastic-flow-oriented layer structures indicate that the microstructural evolution is highly determined by the distribution of shear strain. The corresponding TEM EDS image, Figure 4.4 (b), also shows a clear reduction of elongated Nb phase thickness as it gets closer to the sample surface. However, for the similar sample processed at 200 ℃, there is a structure boundary (highlighted by the white dashed line) between the NC region and the UFG region, as shown in Figure 4.4 (c). The layered structure is not obvious in the sample processed at 200 ℃. The boundary here suggests a critical value of the two competitive mechanisms. Above this line, the high shear deformation induced atomic mixing mechanism is more dominant than the thermal

diffusion of Cu and Nb atoms at 200 ℃. But below this line, the thermal activated mechanism is strong enough for the Cu grain boundaries to glide or move along, resulting in a coarser structure. This assumption is based on the plot showing critical values for the microstructural patterning as a function of these two mechanisms [131]. Figure 4.4 (d1) shows the UFG region below the boundary, and its correlated EDS map (d2) shows an elongated Nb particle (pointed by a white arrow) in the Cu matrix. The RT shear deformation resulted in highly refined distribution of Cu and Nb throughout the wear track, while at 200 ℃ the Nb is very localized and limited to sparse locations. In addition, comparing the APT analysis of the sample processed at RT (embedded in Figure 4.4 (b)) and at 200 ºC (Figure 4.4 (e1) and (e2)), it is indicated that Cu-4at%Nb processed at 200 ºC is oxidized (Supplementary Figure S3 shows the TEM results from 400 ℃ condition depicting severe Cu oxides formation extending to ~2 μm below the wear track). In addition, the embedded EDS map of O in Figure 4.4 (c) also indicates that the sub-surface area of the sample processed at 200 ºC is oxidized. Copper oxides formed at the sub-surface area are being thrown away after attaining certain thickness upon sliding. In addition, some amount of copper oxide is smeared into the track but is not enough to reduce the shear strength of the contact area, leading to more metal-counterface contact area. As a result, CoF and wear rate are increased at 400 ºC compared with that at RT.

In a broad view, due to the characteristics of SPP, materials are self-constrained and remain solid state during shearing. Here, based on the tribological response and microscopy results, the phase specific strain accommodation as a function of total strain and temperature is studied. Friction occurs whenever two solid bodies slide against each other,

where mechanical energy is transformed into internal energy of heat, which causes the temperature of the sliding bodies to increase [132]. The increased temperature within or around the shear zone then affect the mass transportation of atoms, along with the induced shear strain. As a result, the famous Zener-Hollomon parameter [133] can be used to describe the deformation behavior of a material subject to SPP:

$$Z = \dot{\varepsilon} \exp (Q/RT), \tag{4.2}$$

where $\dot{\varepsilon}$ Q is the activation energy, R is the gas constant, and T is the temperature. Based on this equation, increase in strain rate during high shear deformation is considered to have an equivalent effect to that of a decrease in deformation temperature, and vice versa. By processing the tribometer test on an immiscible Cu-Nb alloy at three different temperatures, the value of Z can be expected to reduce as the temperature is increased. In this study, the shear strain applied at various depths and temperature has been estimated by Equation (4.1) and shown in Figure 4.3 (b). T ($\dot{\varepsilon}$we take the activation energy Q of pure Cu to be 72.5 kJ/mol [134]. The Zener-Hollomon parameter lnZ is then calculated based on Equation (4.2) and shown in *Supplementary Figure S4*. The result indicates that lnZ reduces from 28 at RT to 14.4 at 200 ºC and 7 at 400 ºC, and it also reduces as the distance to sample surface is increased. Cui et al. have estimated a range of lnZ from 22 to 66 based on various strain rate and temperatures [135] while Liu et al. measured it to be from 20 to 40 for cold sprayed Cu [136]. Based on our results (*Supplementary Figure S4)*, the Zener-Hollomon parameter of RT tested sample (28) are in the range of previously reported work, while for the samples

tested at 200 ºC (14.4) and 400 ºC (7) it is reduced due to external heating thus implying lesser microstructural refinement during processing at elevated temperatures.

This analysis is consistent with our theory that when external heating is applied, the recrystallized grains and the disappearance of shear-driven lamination structure indicate that atoms tend to "heal" the affected area and eliminate the effects of shear strain. Figure 4.3 (b) provides a quantitative measurement for shear-temperature accommodation. The maximum shear strain reduces from ~200 at RT to ~45 at 200 º C and reduces further down to ~5 at 400 ºC.

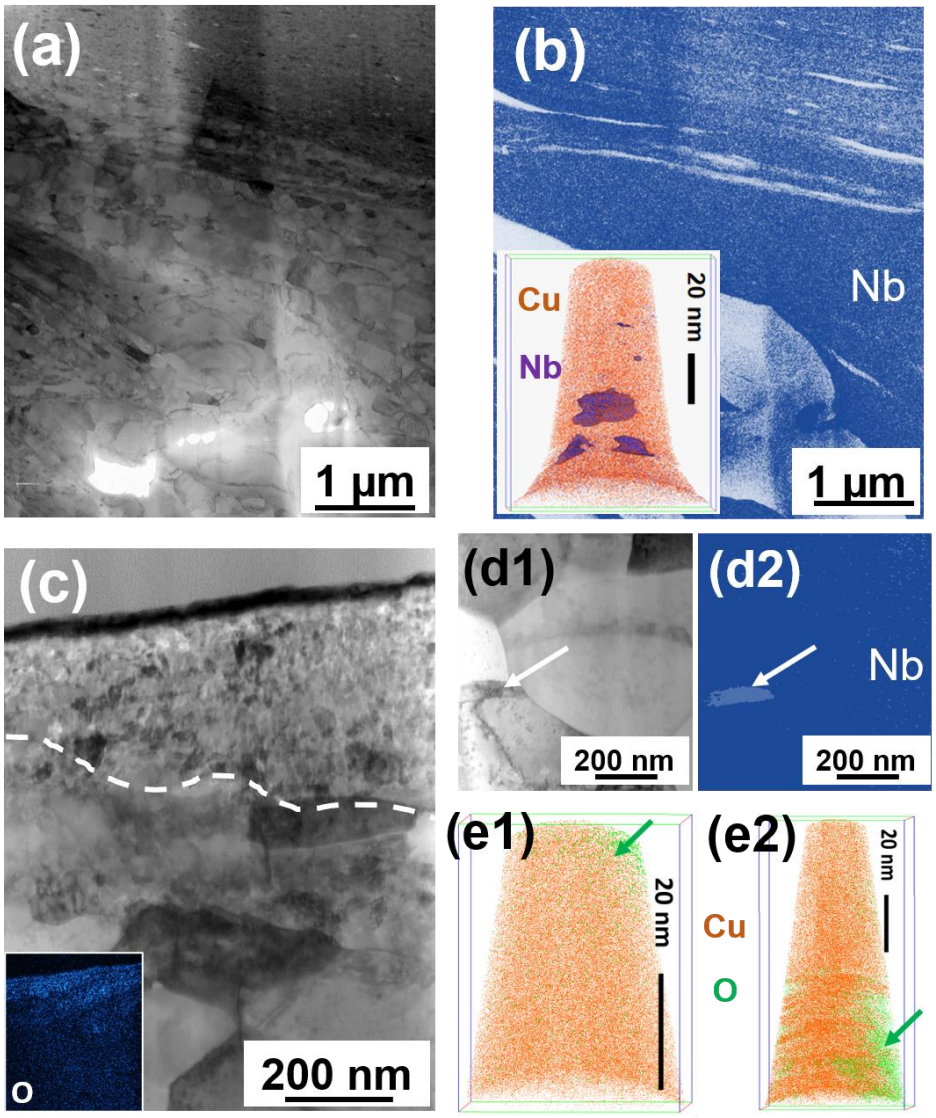

Figure 4.4 (a) BF-TEM image showing microstructural evolution of Cu-4at%Nb processed at RT, (b) EDS map showing the change in Nb particle thickness as a function of depth with an embedded APT reconstruction obtained at ~ 1.2 µm below the wear track consisting of fine-scale Nb rich regions segregating in the Cu matrix, (c) BF-TEM image showing microstructural evolution of Cu-4at%Nb processed at 200ºC with a highlighted boundary separating the NC region and UFG region, and an embedded EDS map of O showing that the closer-to-surface area is more oxidized, (d1) BF-TEM image showing a small elongated Nb particle in the UFG region (pointed by a white arrow), (d2) corresponding EDS mapping showing the Nb particle in the Cu matrix, (e1) APT reconstruction obtained at ~ 1.2 µm below the wear track showing only Cu and O but no Nb, (e2) APT reconstruction obtained at ~ 4.7 µm below the wear track also showing only Cu and O elements but no Nb.

4.5 Conclusions

In summary, in our study the changes in CoF and wear mechanism are related to fine-scale changes in the underlying microstructure of the alloy. The CoFs of the alloy processed at RT (0.51 ± 0.03) and 200 ºC (0.49 ± 0.05) are observed to be in a similar range, but it increases to 0.80 ± 0.05 at 400 ºC, possibly due to formation of Cu oxides particles between the wearing surfaces. The wear rate of the Cu-Nb alloy increases from 0.04 ± 0.03 10^{-4} mm^3/N.m at RT to 0.2 ± 0.05 mm^3/N.m at 200ºC and 0.65 ± 0.07 mm^3/N.m at 400 ºC, indicating that the alloy is not resistant to thermal softening due to grain growth/recrystallization and strain relaxation caused by external heating

Spherical Nb particles, which are unevenly distributed in the as-cast Cu-Nb alloy, are stretched into elongated geometry by a high cyclic shear stress. Extremely high strain at RT results in formation of nanofibers of Nb and a homogeneous redistribution while at high temperature due to limited shear strain, the shear deformation of Nb is limited. The disappearance of the shear driven layered structure indicates that the microstructural evolution for the sample processed at RT is highly determined by the shear strain gradient, while for the sample processed with external heating, temperature is also playing a significant role in it. Electron microscopy and chemical compositional analysis indicate that there are some Cu oxides at 200 ºC and more Cu oxides at 400 ºC, which affects the tribological response of the material. APT analysis shows fine Nb fibers at the NC region in the sample processed at RT, but not at 200 ºC and 400 ºC, indicating that Nb refinement is prohibited by external heating.

Supplementary information

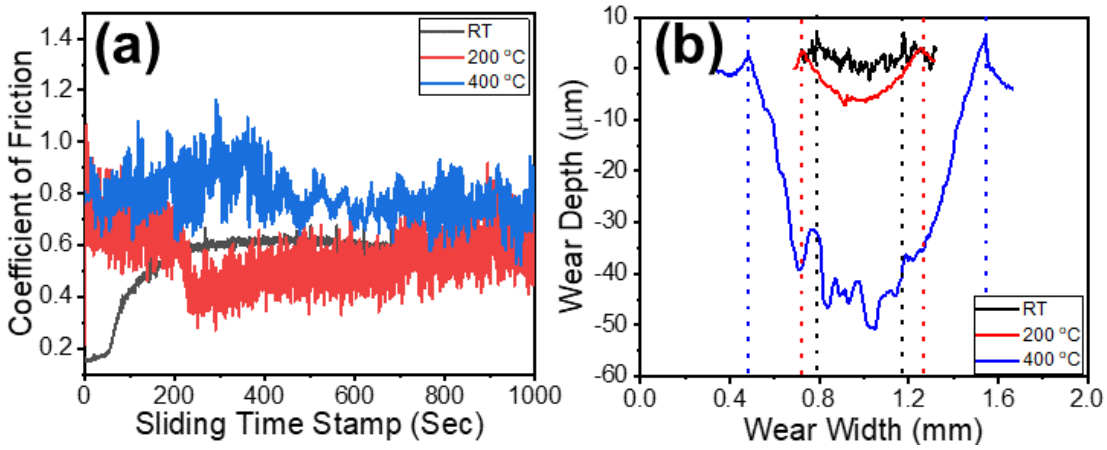

Supplementay Figure S1 (a) Coefficient of friction curve a function of time stamp for the sample processed at RT, 200 ℃, and 400 ℃; (b) 2D cross-sectional representation of wear width and depth of Cu-4at%Nb processed at RT, 200 ℃, and 400 ℃ showing and increase in depth with an increase in temperature. The higher wear rate and deeper wear track at a higher temperature indicate that there is very likely grain growth/recrystallization and strain relaxation caused by external heating. Thus, the softened subsurface material is more scratched away, resulting in a larger material – pin contact area at a higher temperature.

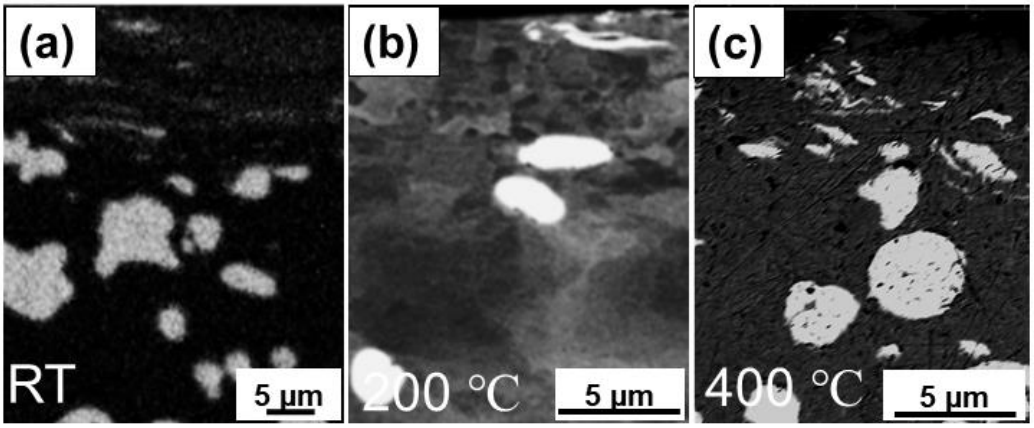

Supplementay Figure S2 SEM images showing reduced Nb particle thickness as it gets closer to the sample surface for Cu-4at%Nb processed at (a) RT, (b) 200 ºC and (c) 400 ºC.

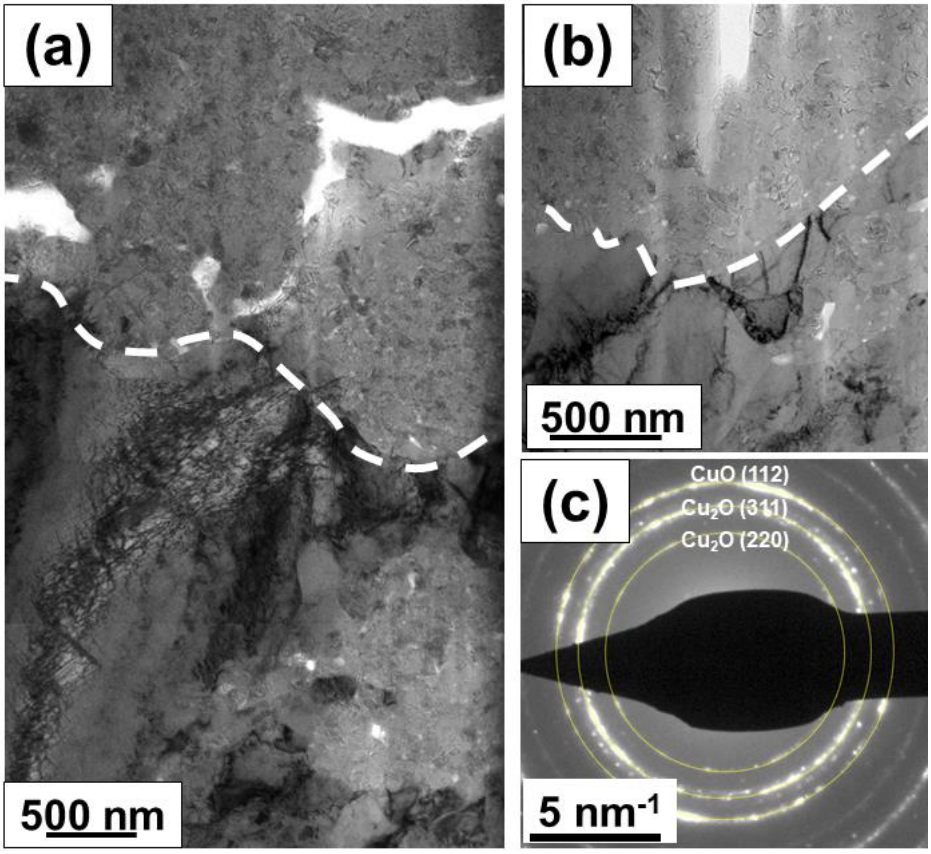

Supplementay Figure S3 Bright-field TEM images showing (a) subsurface microstructure of Cu-4at%Nb processed at 400 ºC, (b) a boundary separating the NC regions and UFG regions, (c) diffraction patterns showing Cu oxides.

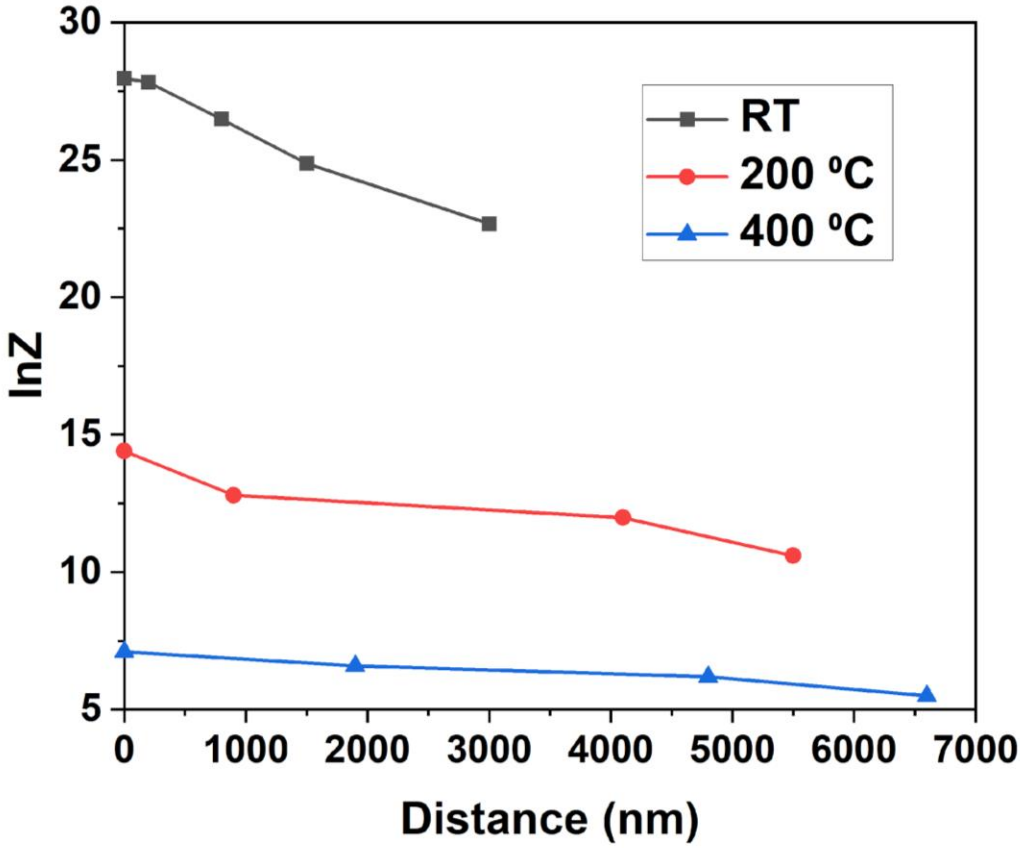

Supplementay Figure S1 Estimated Zener-Hollomon parameter as a function of distance to the sample surface at RT, 200 ºC and 400 ºC.

Conclusions

In conclusion, this dissertation studied the processing - microstructure – property relationship in novel binary NC alloys via two perspective. The first perspective is in an engineering side, where we studied the mechanical response of NC bioresorbable Fe-Mn alloys as a function of processing routes and microstructural evolution compared with their coarse-grained counterparts. The second perspective is in a fundamental science side, where the thermomechanical stability of immiscible Cu-based NC alloys and the

microstructural evolution of an immiscible alloy affected by shear strain and temperature independently are studied.

In the engineering part, both mechanical response and bio performance as a function of microstructure/structure of bioresorbable Fe-30wt%Mn samples are studied by tailoring the processing route. In detail, Fe-30wt%Mn went through shear deformation in various extent by HPT for one, two and four turns, and Fe-30wt%Mn was fabricated by mechanical alloying and consolidated by SPS with three different programs. These tailorable parameters in processing routes resulted in various microstructures/structures of Fe-Mn alloys, which further affected their mechanical response and bio performance. Results show that after one turn of HPT, the microhardness of Fe-Mn alloys increased significantly compared with the initially homogenized sample due to grain refinement and deformation twinning. However, the microhardness did not change significantly after two turns and four turns of HPT indicating dislocation saturation which caused suppression of nano-twinning, dislocation-nanotwin annihilation, and unfavorable grain-orientation for easy slip. After several strengthening mechanisms are discussed, the grain refinement, high dislocation density and deformation twinning are considered dominant in the strengthening model of Fe-30wt%Mn after HPT. Also, Fe-30wt%Mn alloys processed by SPEX mill and SPS are full of tiny porous while the region between initial milled particles is occupied with relatively larger pores. These pores acted as the vulnerable area during static immersion tests and degraded faster than other areas. As a result, it is concluded that with a well-designed mechanical processing and fabrication program, a nano-scale tailorable bioresorbable Fe-30wt%Mn can be achieved.

The second part of this dissertation, from a science perspective, involves fundamental investigation of thermomechanical immiscible Cu-based NC alloys and their microstructural and mechanical behavior affected by severe shear and temperature. NC Cu-Ta alloys made by SPS exhibited a microstructural stability at elevated temperatures or under mechanical loading conditions. The observed bimodality of Ta segregates (Ta particles and Ta nanoclusters) resulted in various strengthening mechanisms to explain the enhanced microhardness of this material. After discussing several potential strengthening mechanisms, it is concluded that the predominant strengthening ones are Hall-Petch effect, Rule-of-mixture strengthening and Zener pinning. Cu-Nb, as another immiscible NC alloy, was used to study the independent contribution of shear strain and temperature on the material during severe shear deformation. Results have shown grain refinement caused by severe shear deformation, as well as grain growth/recrystallization and strain relaxation caused by external heating. Extremely high strain at RT results in formation of nanofibers of Nb and a homogeneous redistribution while at high temperature due to limited shear strain, the shear deformation of Nb is limited. The disappearance of the shear driven layered structure indicates that the microstructural evolution for the sample processed at RT is highly determined by the shear strain gradient, while for the sample processed with external heating, temperature is also playing a significant role in it.

In summary, this dissertation is expected to provide a better understanding on how the mechanical and bio response of NC Fe-Mn alloys affected by processing routes and microstructures, as well as how shear strain and temperature affect the microstructural

evolution and mechanical behavior of thermomechanical stable immiscible Cu-based NC alloys.

Reference

1. Kumar, K., H. Van Swygenhoven, and S. Suresh, *Mechanical behavior of nanocrystalline metals and alloys.* Acta materialia, 2003. **51**(19): p. 5743-5774.

2. Meyers, M.A., A. Mishra, and D.J. Benson, *Mechanical properties of nanocrystalline materials.* Progress in materials science, 2006. **51**(4): p. 427-556.

3. Wei, Q., et al., *Dynamic behaviors of body-centered cubic metals with ultrafine grained and nanocrystalline microstructures.* Materials Science and Engineering: A, 2008. **493**(1-2): p. 58-64.

4. Chookajorn, T., H.A. Murdoch, and C.A. Schuh, *Design of stable nanocrystalline alloys.* Science, 2012. **337**(6097): p. 951-954.

5. Bui, K., T. Hasanali, and T. Goodrich. *New final finish stack including a custom nano-crystalline silver alloy for mobile connector systems with high cycling wear and powered environmental exposure requirements*. in *2015 IEEE 65th Electronic Components and Technology Conference (ECTC)*. 2015. IEEE.

6. Wei, Q., et al., *Microstructure and mechanical properties of super-strong nanocrystalline tungsten processed by high-pressure torsion.* Acta materialia, 2006. **54**(15): p. 4079-4089.

7. Wang, Y., et al., *Microsample tensile testing of nanocrystalline copper.* Scripta Materialia, 2003. **48**(12): p. 1581-1586.

8. Youssef, K.M., et al., *Ultratough nanocrystalline copper with a narrow grain size distribution.* Applied physics letters, 2004. **85**(6): p. 929-931.

9. Liang, X., et al., *Microstructural evolution and strain hardening of Fe–24Mn and Fe–30Mn alloys during tensile deformation.* Acta Materialia, 2009. **57**(13): p. 3978-3988.

10. Heiden, M., D. Johnson, and L. Stanciu, *Surface modifications through dealloying of Fe–Mn and Fe–Mn–Zn alloys developed to create tailorable, nanoporous, bioresorbable surfaces.* Acta Materialia, 2016. **103**: p. 115-127.

11. Yanushkevich, Z., et al., *Structural/textural changes and strengthening of an advanced high-Mn steel subjected to cold rolling.* Materials Science and Engineering: A, 2016. **651**: p. 763-773.

12. Bouaziz, O. and N. Guelton, *Modelling of TWIP effect on work-hardening.* Materials Science and Engineering: A, 2001. **319**: p. 246-249.

13. Volynova, T. and V. Mnasin, *Cold brittleness of industrial purity iron-manganese alloys.* Metal Science and Heat Treatment, 1983. **25**(11): p. 836-843.

14. Ueji, R., et al., *Crystallographic orientation dependence of ε martensite transformation during tensile deformation of polycrystalline 30% Mn austenitic steel.* Materials Science and Engineering: A, 2013. **576**: p. 14-20.

15. Schaffer, J.E., E.A. Nauman, and L.A. Stanciu, *Cold drawn bioabsorbable ferrous and ferrous composite wires: an evaluation of in vitro vascular cytocompatibility.* Acta biomaterialia, 2013. **9**(10): p. 8574-8584.

16. Walker, E.K., et al., *An in vitro model for preclinical testing of thrombogenicity of resorbable metallic stents.* Journal of Biomedical Materials Research Part A, 2015. **103**(6): p. 2118-2125.

17. Schaffer, J.E., E.A. Nauman, and L.A. Stanciu, *Cold-drawn bioabsorbable ferrous and ferrous composite wires: An evaluation of mechanical strength and fatigue durability.* Metallurgical and Materials Transactions B, 2012. **43**(4): p. 984-994.

18. Zhilyaev, A.P. and T.G. Langdon, *Using high-pressure torsion for metal processing: Fundamentals and applications.* Progress in Materials science, 2008. **53**(6): p. 893-979.

19. Mamedov, V., *Spark plasma sintering as advanced PM sintering method.* Powder Metallurgy, 2002. **45**(4): p. 322-328.

20. Gleiter, H., *Nanostructured materials: basic concepts and microstructure.* Acta materialia, 2000. **48**(1): p. 1-29.

21. Chokshi, A., et al., *On the validity of the Hall-Petch relationship in nanocrystalline materials.* Scripta metallurgica, 1989. **23**(10): p. 1679-1684.

22. Padilla, H. and B. Boyce, *A review of fatigue behavior in nanocrystalline metals.* Experimental mechanics, 2010. **50**(1): p. 5-23.

23. Darling, K., et al., *Extreme creep resistance in a microstructurally stable nanocrystalline alloy.* Nature, 2016. **537**(7620): p. 378-381.

24. Darling, K., et al., *Grain size stabilization of nanocrystalline copper at high temperatures by alloying with tantalum.* Journal of Alloys and Compounds, 2013. **573**: p. 142-150.

25. Lee, H.-J., et al., *Thermal stability of a Cu/Ta multilayer: an intriguing interfacial reaction.* Acta materialia, 1999. **47**(15-16): p. 3965-3975.

26. Shuai, C., et al., *Mechanical alloying of immiscible metallic systems: process, microstructure, and mechanism.* Advanced Engineering Materials, 2021. **23**(4): p. 2001098.

27. Escobar, J., et al., *Multimodal Analysis of Spatially Heterogeneous Microstructural Refinement and Softening Mechanisms in Three-Pass Friction Stir Processed Al-4Si Alloy.* Journal of Alloys and Compounds, 2021: p. 161351.

28. Gwalani, B., et al., *Lattice misorientation evolution and grain refinement in Al-Si alloys under high-strain shear deformation.* Materialia, 2021: p. 101146.

29. Patel, V., et al., *Recent development in friction stir processing as a solid-state grain refinement technique: microstructural evolution and property enhancement.* Critical Reviews in Solid State and Materials Sciences, 2019. **44**(5): p. 378-426.

30. Bhushan, B. and M. Nosonovsky, *Scale effects in friction using strain gradient plasticity and dislocation-assisted sliding (microslip).* Acta materialia, 2003. **51**(14): p. 4331-4345.

31. Chee, S., et al., *Dynamic self-organization in Cu alloys under ion irradiation.* Acta Materialia, 2010. **58**(12): p. 4088-4099.

32. Valiev, R.Z. and T.G. Langdon, *Principles of equal-channel angular pressing as a processing tool for grain refinement.* Progress in materials science, 2006. **51**(7): p. 881-981.

33. Tamadon, A., et al., *Thermomechanical grain refinement in AA6082-T6 thin plates under Bobbin friction stir welding.* Metals, 2018. **8**(6): p. 375.

34. Charit, I. and R.S. Mishra, *Abnormal grain growth in friction stir processed alloys.* Scripta materialia, 2008. **58**(5): p. 367-371.

35. Akbari, M., et al., *Investigation of the effect of friction stir processing parameters on temperature and forces of Al–Si aluminum alloys.* Proceedings of the Institution of Mechanical Engineers, Part L: Journal of Materials: Design and Applications, 2018. **232**(3): p. 213-229.

36. Grässel, O., et al., *High strength Fe–Mn–(Al, Si) TRIP/TWIP steels development—properties—application.* International Journal of plasticity, 2000. **16**(10-11): p. 1391-1409.

37. Cullity, B.D., *Elements of X-ray Diffraction*. 1956: Addison-Wesley Publishing.
38. Saeed-Akbari, A., A. Schwedt, and W. Bleck, *Low stacking fault energy steels in the context of manganese-rich iron-based alloys.* Scripta Materialia, 2012. **66**(12): p. 1024-1029.

39. Sadia, Y. and Y. Gelbstein, *Silicon-rich higher manganese silicides for thermoelectric applications.* Journal of electronic materials, 2012. **41**(6): p. 1504-1508.

40. Lugo, N., et al., *Microstructures and mechanical properties of pure copper deformed severely by equal-channel angular pressing and high pressure torsion.* Materials Science and Engineering: A, 2008. **477**(1-2): p. 366-371.

41. Yang, P., et al., *Dependence of deformation twinning on grain orientation in a high manganese steel.* Scripta Materialia, 2006. **55**(7): p. 629-631.

42. Hansen, N., X. Huang, and D. Hughes, *Microstructural evolution and hardening parameters.* Materials Science and Engineering: A, 2001. **317**(1-2): p. 3-11.

43. Hughes, D. and N. Hansen, *High angle boundaries formed by grain subdivision mechanisms.* Acta materialia, 1997. **45**(9): p. 3871-3886.

44. Meng, L., et al., *Dependence of deformation twinning on grain orientation in compressed high manganese steels.* Scripta Materialia, 2007. **56**(11): p. 931-934.

45. Frommeyer, G., U. Brüx, and P. Neumann, *Supra-ductile and high-strength manganese-TRIP/TWIP steels for high energy absorption purposes.* ISIJ international, 2003. **43**(3): p. 438-446.

46. Harai, Y., et al., *Microstructural and mechanical characteristics of AZ61 magnesium alloy processed by high-pressure torsion.* Materials transactions, 2008. **49**(1): p. 76-83.

47. Belyakov, A., et al., *Microstructure evolution in ferritic stainless steels during large strain deformation.* Materials transactions, 2004. **45**(9): p. 2812-2821.

48. Edalati, K., et al., *High-pressure torsion of pure magnesium: Evolution of mechanical properties, microstructures and hydrogen storage capacity with equivalent strain.* Scripta Materialia, 2011. **64**(9): p. 880-883.

49. Park, B.H., et al., *Large deformation behavior of twin-induced plasticity steels under high-pressure torsion.* Metals and Materials International, 2016. **22**(6): p. 1003-1008.

50. Astafurova, E., et al., *Microstructure and mechanical response of single-crystalline high-manganese austenitic steels under high-pressure torsion: The effect of stacking-fault energy.* Materials Science and Engineering: A, 2014. **604**: p. 166-175.

51. Kashyap, K., et al., *On peierls nabarro stress in iron.* Computational materials science, 2012. **56**: p. 172-173.

52. Bouaziz, O., S. Allain, and C. Scott, *Effect of grain and twin boundaries on the hardening mechanisms of twinning-induced plasticity steels.* Scripta Materialia, 2008. **58**(6): p. 484-487.

53. Kim, J.G., et al., *Superior strength and multiple strengthening mechanisms in nanocrystalline TWIP steel.* Scientific reports, 2018. **8**(1): p. 1-10.

54. De las Cuevas, F., et al. *Hall-Petch relationship of a TWIP steel*. in *Key Engineering Materials*. 2010. Trans Tech Publ.

55. Ganji, R.S., et al., *Strengthening mechanisms in equiatomic ultrafine grained AlCoCrCuFeNi high-entropy alloy studied by micro-and nanoindentation methods.* Acta Materialia, 2017. **125**: p. 58-68.

56. Hermawan, H., D. Ramdan, and J.R. Djuansjah, *Metals for biomedical applications.* Biomedical engineering-from theory to applications, 2011. **1**: p. 411-430.

57. Vidal, C.V. and A.I. Muñoz, *Electrochemical characterisation of biomedical alloys for surgical implants in simulated body fluids.* Corrosion Science, 2008. **50**(7): p. 1954-1961.

58. Di Mario, C., et al., *Drug-eluting bioabsorbable magnesium stent.* Journal of interventional cardiology, 2004. **17**(6): p. 391-395.

59. Thierry, B., et al., *Nitinol versus stainless steel stents: acute thrombogenicity study in an ex vivo porcine model.* Biomaterials, 2002. **23**(14): p. 2997-3005.

60. Migliavacca, F., et al., *Stainless and shape memory alloy coronary stents: a computational study on the interaction with the vascular wall.* Biomechanics and Modeling in Mechanobiology, 2004. **2**(4): p. 205-217.

61. Pogorielov, M., et al., *Magnesium-based biodegradable alloys: Degradation, application, and alloying elements.* Interventional Medicine and Applied Science, 2017. **9**(1): p. 27-38.

62. Waksman, R., et al., *Safety and efficacy of bioabsorbable magnesium alloy stents in porcine coronary arteries.* Catheterization and Cardiovascular Interventions, 2006. **68**(4): p. 607-617.

63. Pierson, D., et al., *A simplified in vivo approach for evaluating the bioabsorbable behavior of candidate stent materials.* Journal of Biomedical Materials Research Part B: Applied Biomaterials, 2012. **100**(1): p. 58-67.

64. Hermawan, H., D. Dubé, and D. Mantovani, *Developments in metallic biodegradable stents.* Acta biomaterialia, 2010. **6**(5): p. 1693-1697.

65. Waksman, R., et al., *Short-term effects of biocorrodible iron stents in porcine coronary arteries.* Journal of interventional cardiology, 2008. **21**(1): p. 15-20.

66. Hermawan, H., et al., *Fe–Mn alloys for metallic biodegradable stents: degradation and cell viability studies.* Acta biomaterialia, 2010. **6**(5): p. 1852-1860.

67. Youn, S.W., et al., *Effect of Manganese Content on the Magnetic Susceptibility of Ferrous-Manganese Alloys: Correlation between Microstructure on X-Ray Diffraction and Size of the Low-Intensity Area on MRI.* Investigative Magnetic Resonance Imaging, 2015. **19**(2): p. 76-87.

68. Hermawan, H., D. Dubé, and D. Mantovani, *Degradable metallic biomaterials: design and development of Fe–Mn alloys for stents.* Journal of Biomedical Materials Research Part A: An Official Journal of The Society for Biomaterials, The Japanese Society for Biomaterials, and The Australian Society for Biomaterials and the Korean Society for Biomaterials, 2010. **93**(1): p. 1-11.

69. Li, H., Y. Zheng, and L. Qin, *Progress of biodegradable metals.* Progress in Natural Science: Materials International, 2014. **24**(5): p. 414-422.

70. Kutscher, H.L., et al., *Threshold size for optimal passive pulmonary targeting and retention of rigid microparticles in rats.* Journal of Controlled Release, 2010. **143**(1): p. 31-37.

71. Zheng, Y.F., X.N. Gu, and F. Witte, *Biodegradable metals.* Materials Science and Engineering: R: Reports, 2014. **77**: p. 1-34.

72. Mattila, P.K. and P. Lappalainen, *Filopodia: molecular architecture and cellular functions.* Nature reviews Molecular cell biology, 2008. **9**(6): p. 446-454.

73. Alves, S.F. and T. Wassall, *In vitro evaluation of osteoblastic cell adhesion on machined osseointegrated implants.* Brazilian oral research, 2009. **23**: p. 131-136.

74. Ryan, G., A. Pandit, and D.P. Apatsidis, *Fabrication methods of porous metals for use in orthopaedic applications.* Biomaterials, 2006. **27**(13): p. 2651-2670.

75. Kokubo, T. and H. Takadama, *How useful is SBF in predicting in vivo bone bioactivity?* Biomaterials, 2006. **27**(15): p. 2907-2915.

76. Dehestani, M., et al., *Effects of microstructure and heat treatment on mechanical properties and corrosion behavior of powder metallurgy derived Fe–30Mn alloy.* Materials Science and Engineering: A, 2017. **703**: p. 214-226.

77. Mote, V., Y. Purushotham, and B. Dole, *Williamson-Hall analysis in estimation of lattice strain in nanometer-sized ZnO particles.* Journal of theoretical and applied physics, 2012. **6**(1): p. 1-8.

78. KANETSUKI, Y., M. KATSUMATA, and T. INOUE, *Relation Between Fine Ferrite-Pearlite Microstructure Produced by Controlled Rolling and Cooling and the Subsequent Rapid Spheroidization of Medium Carbon Steel.* Tetsu-to-Hagane, 1990. **76**(1): p. 73-80.

79. Tsuji, N. and T. Maki, *Enhanced structural refinement by combining phase transformation and plastic deformation in steels.* Scripta Materialia, 2009. **60**(12): p. 1044-1049.

80. Ueji, R., et al., *Ultragrain refinement of plain low carbon steel by cold-rolling and annealing of martensite.* Acta Materialia, 2002. **50**(16): p. 4177-4189.

81. Takaki, S., et al., *Effect of grain refinement on thermal stability of metastable austenitic steel.* Materials Transactions, 2004. **45**(7): p. 2245-2251.

82. Tomota, Y., M. Strum, and J. Morris, *Microstructural dependence of Fe-high Mn tensile behavior.* Metallurgical Transactions A, 1986. **17**(3): p. 537-547.

83. Venables, J., *The martensite transformation in stainless steel.* The Philosophical Magazine: A Journal of Theoretical Experimental and Applied Physics, 1962. **7**(73): p. 35-44.

84. Heiden, M., et al., *Effect of microstructure and strain on the degradation behavior of novel bioresorbable iron–manganese alloy implants.* Journal of Biomedical Materials Research Part A, 2015. **103**(2): p. 738-745.

85. Vandrovcová, M. and L. Bacakova, *Adhesion, growth and differentiation of osteoblasts on surface-modified materials developed for bone implants.* Physiological Research, 2011. **60**(3): p. 403.

86. Murphy, C.M., M.G. Haugh, and F.J. O'brien, *The effect of mean pore size on cell attachment, proliferation and migration in collagen–glycosaminoglycan scaffolds for bone tissue engineering.* Biomaterials, 2010. **31**(3): p. 461-466.

87. Bhatia, M., et al., *The role of Ta on twinnability in nanocrystalline Cu–Ta alloys.* Materials Research Letters, 2017. **5**(1): p. 48-54.

88. Hornbuckle, B., et al., *Effect of Ta solute concentration on the microstructural evolution in immiscible Cu-Ta alloys.* Jom, 2015. **67**(12): p. 2802-2809.

89. Darling, K.A., S. Mathaudhu, and L. Kecskes, *Demonstration of Ultra High-Strength Nanocrystalline Copper Alloys for Military Applications*. 2012, ARMY RESEARCH LAB ABERDEEN PROVING GROUND MD.

90. Fang, Q., et al., *Microstructures and mechanical properties of spark plasma sintered Cu–Cr composites prepared by mechanical milling and alloying.* Materials & Design, 2015. **88**: p. 8-15.

91. Saheb, N., et al., *Spark plasma sintering of metals and metal matrix nanocomposites: a review.* Journal of Nanomaterials, 2012. **2012**.

92. Tschopp, M.A., et al., *"Bulk" nanocrystalline metals: review of the current state of the art and future opportunities for copper and copper alloys.* Jom, 2014. **66**(6): p. 1000-1019.

93. Furukawa, M., et al., *Processing of metals by equal-channel angular pressing.* Journal of materials science, 2001. **36**(12): p. 2835-2843.

94. Zhang, Z., et al., *Microstructure characteristic, mechanical properties and sintering mechanism of nanocrystalline copper obtained by SPS process.* Materials Science and Engineering: A, 2009. **523**(1-2): p. 134-138.

95. Rajagopalan, M., et al., *Microstructural evolution in a nanocrystalline Cu-Ta alloy: a combined in-situ TEM and atomistic study.* Materials & design, 2017. **113**: p. 178-185.

96. Turnage, S., et al., *Anomalous mechanical behavior of nanocrystalline binary alloys under extreme conditions.* Nature communications, 2018. **9**(1): p. 1-10.

97. Darling, K., et al., *Microstructure and mechanical properties of bulk nanostructured Cu–Ta alloys consolidated by equal channel angular extrusion.* Acta materialia, 2014. **76**: p. 168-185.

98. Rahmanifard, R., S.M. Javidan, and M.A. Asadabad, *Effect of Ta content and sintering temperature on characteristics of nanocrystalline Cu-Ta nanocomposite.* Applied Physics A, 2020. **126**(9): p. 1-9.

99. Donnelly, M. and R. Haynes, *MEASUREMENT OF THE DENSITY AND POROSITY OF SMALL SPECIMENS OF LOW POROSITY BY A FLOTATION METHOD.* Powder Metallurgy, 1972. **15**(29): p. 11-16.

100. Frolov, T., et al., *Stabilization and strengthening of nanocrystalline copper by alloying with tantalum.* Acta Materialia, 2012. **60**(5): p. 2158-2168.

101. Zhang, Z.-H., et al., *Ultrafine-grained copper prepared by spark plasma sintering process.* Materials Science and Engineering: A, 2008. **476**(1-2): p. 201-205.

102. Sanders, P.G., J. Eastman, and J. Weertman, *Elastic and tensile behavior of nanocrystalline copper and palladium.* Acta materialia, 1997. **45**(10): p. 4019-4025.

103. Suryanarayana, C., E. Ivanov, and V. Boldyrev, *The science and technology of mechanical alloying.* Materials Science and Engineering: A, 2001. **304**: p. 151-158.

104. Kale, C., et al., *Thermo-mechanical strengthening mechanisms in a stable nanocrystalline binary alloy–A combined experimental and modeling study.* Materials & Design, 2019. **163**: p. 107551.

105. Rojhirunsakool, T., et al., *Structure and thermal decomposition of a nanocrystalline mechanically alloyed supersaturated Cu-Ta solid solution.* MRS Communications, 2015. **5**(2): p. 333.

106. Subramanian, P. and D. Laughlin, *The Cu-Ta (copper-tantalum) system.* Bulletin of alloy phase diagrams, 1989. **10**(6): p. 652-655.

107. Müller, C.M. and R. Spolenak, *An in situ X-ray diffraction study of phase separation in Cu–Ta alloy thin films.* Thin Solid Films, 2016. **598**: p. 276-288.

108. Koju, R., et al., *Zener pinning of grain boundaries and structural stability of immiscible alloys.* Jom, 2016. **68**(6): p. 1596-1604.

109. Courtney, T.H., *Mechanical behavior of materials*. 2005: Waveland Press.

110. Atwater, M.A., et al., *The thermal stability of nanocrystalline copper cryogenically milled with tungsten.* Materials Science and Engineering: A, 2012. **558**: p. 226-233.

111. Schuster, B., et al., *Nanocrystalline refractory metals for extreme condition applications.* Jom, 2011. **63**(12): p. 27-31.

112. PA, M., M. Ferry, and T. Chandra, *Five decades of the Zener equation.* ISIJ international, 1998. **38**(9): p. 913-924.

113. Pun, G.P., et al., *Angular-dependent interatomic potential for the Cu–Ta system and its application to structural stability of nano-crystalline alloys.* Acta Materialia, 2015. **100**: p. 377-391.

114. Özerinç, S., et al., *Grain boundary doping strengthens nanocrystalline copper alloys.* Scripta Materialia, 2012. **67**(7-8): p. 720-723.

115. Steigman, J., W. Shockley, and F. Nix, *The self-diffusion of copper.* Physical Review, 1939. **56**(1): p. 13.

116. Kuper, A., et al., *Self-diffusion in copper.* Physical Review, 1954. **96**(5): p. 1224.

117. Dalla Torre, F., et al., *Microstructures and properties of copper processed by equal channel angular extrusion for 1–16 passes.* Acta materialia, 2004. **52**(16): p. 4819-4832.

118. Taylor, G.I., *The mechanism of plastic deformation of crystals. Part I.—Theoretical.* Proceedings of the Royal Society of London. Series A, Containing Papers of a Mathematical and Physical Character, 1934. **145**(855): p. 362-387.

119. Haouaoui, M., et al., *Microstructure evolution and mechanical behavior of bulk copper obtained by consolidation of micro-and nanopowders using equal-channel angular extrusion.* Metallurgical and materials transactions A, 2004. **35**(9): p. 2935-2949.

120. Qiu, X., et al., *Effect of intrinsic lattice resistance in strain gradient plasticity.* Acta Materialia, 2001. **49**(19): p. 3949-3958.

121. Wang, H., M. Zaluzec, and J. Rigsbee, *Microstructure and mechanical properties of sputter-deposited Cu 1− x Ta x alloys.* Metallurgical and Materials Transactions A, 1997. **28**(4): p. 917-925.

122. Raeker, E., M. Powers, and A. Misra, *Mechanical performance of co-deposited immiscible Cu–Ta thin films.* Scientific Reports, 2020. **10**(1): p. 1-10.

123. Wang, F., et al., *Shear banding deformation in Cu/Ta nano-multilayers.* Materials Science and Engineering: A, 2011. **528**(24): p. 7290-7294.

124. Müller, C.M., et al., *The as-deposited structure of co-sputtered Cu–Ta alloys, studied by X-ray diffraction and molecular dynamics simulations.* Acta Materialia, 2015. **82**: p. 51-63.

125. Cai, W. and P. Bellon, *Effect of annealing treatment on the dry sliding wear behavior of copper.* Wear, 2019. **426**: p. 1187-1194.

126. Vergne, C., et al., *Analysis of the friction and wear behavior of hot work tool scale: application to the hot rolling process.* Wear, 2001. **250**(1-12): p. 322-333.

127. Barrau, O., et al., *Analysis of the friction and wear behaviour of hot work tool steel for forging.* Wear, 2003. **255**(7-12): p. 1444-1454.

128. Pradeep Kumar, J., *Effect of temperature distribution in ultrasonically welded joints of copper wire and sheet used for electrical contacts.* Materials, 2018. **11**(6): p. 1010.

129. Dautzenberg, J. and J. Zaat, *Quantitative determination of deformation by sliding wear.* Wear, 1973. **23**(1): p. 9-19.

130. Bharat Gwalani, A.Y., Krassimir Bozhilov, Christian Roach, Cynthia A. Powell, Suveen Mathaudhu, Aashish Rohatgi, Arun Devaraj, *Experimental and computational approaches uncovering the trans-formation pathway for co-deformation of immiscible metallic phases under severe shear deformation.* Materialia, 2021.

131. Enrique, R.A. and P. Bellon, *Compositional patterning in systems driven by competing dynamics of different length scale.* Physical review letters, 2000. **84**(13): p. 2885.

132. Bhushan, B., *Frictional heating and contact temperatures*, in *Modern Tribology Handbook, Two Volume Set*. 2000, CRC Press. p. 265-302.

133. Medina, S.F. and C.A. Hernandez, *General expression of the Zener-Hollomon parameter as a function of the chemical composition of low alloy and microalloyed steels.* Acta materialia, 1996. **44**(1): p. 137-148.

134. Mishra, A., et al., *Microstructural evolution in copper subjected to severe plastic deformation: Experiments and analysis.* Acta Materialia, 2007. **55**(1): p. 13-28.

135. Li, Y., et al., *Effect of the Zener–Hollomon parameter on the microstructures and mechanical properties of Cu subjected to plastic deformation.* Acta Materialia, 2009. **57**(3): p. 761-772.

136. Liu, Z., et al., *Prediction of heterogeneous microstructural evolution in cold sprayed copper coatings using local Zener-Hollomon parameter and strain.* Acta Materialia, 2020. **193**: p. 191-201.